



The GIEMS-MethaneCentric database: a dynamic and comprehensive global product of methane-emitting aquatic areas

Juliette Bernard^{1,2}, Catherine Prigent^{1,3}, Carlos Jimenez^{3,1}, Etienne Fluet-Chouinard⁴, Bernhard Lehner⁵, Elodie Salmon², Philippe Ciais², Zhen Zhang⁶, Shushi Peng⁷, and Marielle Saunois²

¹LERMA, Paris Observatory, CNRS, PSL, Paris, France

²Laboratoire des Sciences du Climat et de l'Environnement, LSCE-IPSL (CEA-CNRS-UVSQ),
Université Paris-Saclay, 91191 Gif-sur-Yvette, France

³Estellus, Paris, France

⁴Earth System Sciences Division, Pacific Northwest National Laboratory, Richland, WA, USA

⁵Department of Geography, McGill University, Montreal, QC H3A 0B9, Canada

⁶Institute of Tibetan Plateau Research, Chinese Academy of Sciences, Beijing, China

⁷College of Urban and Environmental Sciences, Peking University, Beijing 100871, China

Correspondence: Juliette Bernard (juliette.bernard@obspm.fr) and Catherine Prigent (catherine.prigent@obspm.fr)

Received: 11 October 2024 – Discussion started: 17 October 2024

Revised: 6 March 2025 – Accepted: 20 March 2025 – Published: 28 June 2025

Abstract. The Global Inundation Extent from Multi-Satellites (GIEMS) database first published in 2001 was a key advance toward the accurate representation of wetlands globally by providing dynamic time series of global surface water based on passive microwave observations. This study supplements the second version of GIEMS (GIEMS-2) with other datasets to produce GIEMS-MethaneCentric (GIEMS-MC), a dynamically mapped dataset of methane-emitting waterlogged and inundated ecosystems. We separated open water from wetlands in GIEMS-MC by using the Global Lakes and Wetlands Database version 2 (GLWDv2) while adding unsaturated peatland areas undetected by GIEMS-2. Rice paddies are identified using the Monthly Irrigated and Rainfed Crop Areas (MIRCA2000) product. A specific coastal zone filtering is applied to avoid ocean artifacts while preserving coastal wetlands. GIEMS-MC covers the period 1992–2020 on a monthly scale at $0.25^\circ \times 0.25^\circ$ spatial resolution. The GIEMS-MC product includes two layers of monthly wetland time series – one for flooded and saturated wetlands and another for all wetlands and peatlands – together with seven layers of compatible static maps of open water bodies (lakes, rivers, reservoirs) and seasonal rice paddy maps used in its production. The dominant vegetation and wetland types per pixel are also provided in GIEMS-MC variables. GIEMS-MC is compared to Wetland Area and Dynamics for Methane Modelling (WAD2M), a dataset providing dynamic wetland information. In terms of wetland extent, all wetlands and peatlands in GIEMS-MC and WAD2M show similar results, with a mean annual maximum of 7.7 Mkm^2 for GIEMS-MC and 6.8 Mkm^2 for WAD2M, with similar spatial patterns in most regions. The GIEMS-MC seamless time series represents a significant advance in wetland representation for methane modelling, although limitations remain in the accurate identification of rice, coastal, and peatland areas. This resource provides harmonized dynamic maps of aquatic methane-emitting surfaces and is available at <https://doi.org/10.5281/zenodo.13919644> (Bernard et al., 2024a).

1 Introduction

Following a stable period from 1999 to 2006, atmospheric methane levels have started to rise again, reaching a record growth rate of $+18 \text{ ppb yr}^{-1}$ in 2021 (Lan et al., 2024). This increase is a cause for concern, particularly given that anthropogenic emissions of this potent greenhouse gas account for approximately one-third of the human-induced radiative forcing (Szopa et al., 2021). As a chemically active greenhouse gas with multiple, time-varying sources and sinks (Saunio et al., 2025), closing the methane budget is challenging. The causes of the observed increase in atmospheric methane remain uncertain. Potential factors include increased human or natural emissions, reduced sinks, or a combination of these factors. However, isotopic evidence suggests that biogenic sources (livestock, wetlands, waste, etc.) may play a significant role in the observed increase (Nisbet et al., 2016, 2019).

Among the sources, natural emissions from wetlands and freshwater ecosystems account for 145 to $369 \text{ Tg CH}_4 \text{ yr}^{-1}$, i.e. 25 % to 51 % of global methane emissions (Saunio et al., 2025). Wetland emissions show significant inter-annual variability (Bousquet et al., 2006; Bridgman et al., 2013) and are sensitive to climate (Bridgman et al., 2013; Zhang et al., 2023). Thus, better understanding natural methane emissions variability in the past will inform future predictions of wetland emissions and their feedback on climate. Large uncertainties remain for both wetlands and freshwater ecosystems methane emissions (Saunio et al., 2020; Canadell et al., 2021). This is due to the difficulty in modelling methane fluxes, which depend on many biotic and abiotic factors (Bridgman et al., 2013; Ge et al., 2024), to the small number of flux observations (Canadell et al., 2021), and to uncertainties in wetland and freshwater area (Bridgman et al., 2013; Melton et al., 2013; Saunio et al., 2020; Canadell et al., 2021), including issues of double counting, where the same area may be counted twice under different categories, inflating estimated emissions (Canadell et al., 2021; Thornton et al., 2016). Yet the area covered by seasonal wetlands remains the single largest source of uncertainty in wetland CH_4 emissions (Melton et al., 2013; Peltola et al., 2019; Poulter et al., 2017; Zhang et al., 2017).

The first global wetland map was produced by Matthews and Fung (1987), providing composite static information on wetland types. Since then, new static wetland products have been established, either from composite information (Lehner and Döll, 2004; Tootchi et al., 2019; Tuanmu and Jetz, 2014) or from remote sensing approaches (Loveland et al., 2000; Friedl et al., 2002; Carroll et al., 2009; Feng et al., 2016; Bartholomé Belward, 2005). Further datasets have been developed based on hydrological model outputs (Ringeval et al., 2012; Wania et al., 2013; Xi et al., 2022), presenting their advantages and disadvantages compared to satellite-derived products. Those models can be used both to reconstruct the historical distribution of wetlands and to

predict their future evolution. Modelling can be an effective method for producing a global map of wetlands, particularly where physics-based models can reflect the mechanisms by which wetlands are formed. The two main limitations of these model outputs are (1) that hydrological models are simplified representations of the real-world complexity of wetlands (e.g. models often focus on a single water surface generation process (Obled and Zin, 2004)) and (2) that human interference is not well accounted for in the models (Hu et al., 2017). Moreover, observations are required to constrain and/or validate these model predictions.

However, there are only a few available observational dynamic time series of surface water maps at a global scale. Notably, these include (1) the Global Inundation Extent from Multi-Satellites (GIEMS and GIEMS-2) (Prigent et al., 2001, 2007; Papa et al., 2010; Prigent et al., 2020) and its downscaled versions (Fluet-Chouinard et al., 2015; Aires et al., 2017) and (2) the Surface Water Microwave Product Series (SWAMPS) (Schroeder et al., 2015; Jensen and McDonald, 2019).

GIEMS-2 and SWAMPS both provide monthly fractions of surface water at $0.25^\circ \times 0.25^\circ$ for 1992–2020, mainly based on passive microwave observations from Special Sensor Microwave Imager (SSM/I) and the Special Sensor Microwave Imager Sounder (SSMIS). Although SWAMPS and GIEMS-2 both aim to represent both inundated surfaces and are produced using similar input data, they present significant differences both in terms of spatial distribution and inter-annual variations (Pham-Duc et al., 2017; Bernard et al., 2024b).

GIEMS-2 and SWAMPS products do not differentiate surface water categories, e.g. wetland, lake, reservoir, pond, or rice paddy, and are therefore not directly usable for wetland studies modelling seasonally inundated wetlands separately from open water bodies. Recent efforts have been made by Zhang et al. (2021b) to produce the Wetland Area and Dynamics for Methane Modeling (WAD2M) product based on SWAMPS, which represents a pioneering attempt to dynamically map wetlands, including peatlands. Using additional high-resolution static estimates of wetlands and open permanent water, as well as seasonal information on rice paddies, Zhang et al. (2021b) were able to apply these correction layers to SWAMPS to distinguish wetlands from other surface water. WAD2M version 2.0 (Zhang et al., 2021a) provides monthly estimates on a global scale for 2000–2020 at $0.25^\circ \times 0.25^\circ$. However, WAD2M has encountered difficulties in capturing reliable inter-annual trends (Zhang et al., 2021b; Bernard et al., 2024b). In fact, issues in SWAMPS are propagated into WAD2M, such as ocean and desert artifacts leading to overestimation and abrupt changes in time series partly due to changes in satellites (Pham-Duc et al., 2017; Bernard et al., 2024b).

In an attempt to compare the corrected wetland extent of WAD2M and GIEMS, McNicol et al. (2023) applied the same correction layers to GIEMS-2, but this exercise did not

eliminate the large differences between these two datasets. In particular, the WAD2M procedure rescales the SWAMPS surface water extent fractions, which are always positive, with other high-resolution static wetland datasets, which potentially produces some unreliable seasonality where the wetland fractions in SWAMPS are below the instrumental noise level. On the contrary, GIEMS-2 shows some zero fractions over numerous pixels where no water is detected. This makes it impossible to use the same procedure as in Zhang et al. (2021b) to produce WAD2M from SWAMPS. The correction procedure needs to be modified to adapt to GIEMS-2. Furthermore, since the release of WAD2M, the most recent maps of aquatic ecosystems have been aggregated into the Global Lakes and Wetlands Database version 2 (GLWDv2), which now offers the most comprehensive and up-to-date representation of global wetland classes (Lehner et al., 2025a).

This study presents a new comprehensive database of methane-emitting surfaces, named the Global Inundation Extent from Multi-Satellites-MethaneCentric (GIEMS-MC). GIEMS-MC aims at providing spatially and dynamically consistent maps of the different methane-emitting ecosystems, with the purpose of providing data for modelling methane emissions at the global scale ($0.25^\circ \times 0.25^\circ$) over 1992–2020. In particular, two time series of wetland maps are developed at a monthly timescale: inundated and saturated wetlands (ISW) and all wetlands including non-inundated peatlands (inundated and saturated wetlands + peatlands, ISW+P). GIEMS-MC also provides compatible information from the ancillary data used, including static surface extents of open permanent waters (lakes, rivers, reservoirs, estuaries, deltas) and seasonal surface extents of rice paddies, along with dominant vegetation on wetland classes. GIEMS-MC takes advantage of the GIEMS-2 product that offers ~ 30 -year seamless time series of surface water with realistic seasonality and inter-annuality (Prigent et al., 2020; Bernard et al., 2024b) and largely benefits from the recently developed comprehensive static map of GLWDv2 (Lehner et al., 2025a). This article outlines the methodology behind the production of GIEMS-MC and provides an analysis and comparison with existing datasets: WAD2M (Zhang et al., 2021b), GLWDv2 (Lehner et al., 2025a), and the original GIEMS-2 (Prigent et al., 2020). Two inundation products based on Cyclone Global Navigation Satellite System (CYGNSS) data are also used for comparison over the Sudd (Zeiger et al., 2023; Gerlein-Safdi et al., 2021). The sensitivity of the wetland estimates to the different process steps is also discussed.

2 Datasets

This section presents the three types of data used in the production of GIEMS-MC: (1) the surface data of the different aquatic ecosystems, (2) the data used for the masks and ad-

ditional ecosystem layers, and (3) the WAD2M comparison dataset.

2.1 Input datasets to GIEMS-MC (GIEMS-2, GLWDv2, MIRCA2000)

The GIEMS-2 dataset, spanning 1992 to 2015 and extended to 2020 in this study, provides monthly global maps of surface water extent with a spatial resolution of $0.25^\circ \times 0.25^\circ$ (Prigent et al., 2020). GIEMS-2 includes all continental water surfaces, such as wetlands, rice paddies, rivers, reservoirs, and lakes, but excludes large lakes ($> 15\,000\text{ km}^2$). The original GIEMS-1 methodology (Prigent et al., 2001, 2007; Papa et al., 2006, 2008, 2010) and the GIEMS-2 algorithm (Prigent et al., 2020; Bernard et al., 2024b) have been extensively evaluated against other observational products, demonstrating robust capture of seasonal and inter-annual variability, despite uncertainties in wetland extent between currently available products. GIEMS-2 relies primarily on inter-calibrated passive microwave observations from the SSM/I and SSMIS satellites (Fennig et al., 2020) at frequencies from 19 to 85 GHz. The microwave signal is influenced by atmospheric conditions (e.g. water vapour, clouds) and surface variables (e.g. surface temperature, vegetation, snow) by other ancillary information to limit these artifacts, as described in Prigent et al. (2020). Microwave observations are complemented by other satellite information to limit these artifacts, as described in Prigent et al. (2020). Specifically, active microwave satellite data and the normalized difference vegetation index (NDVI) derived from visible and near-infrared measurements are used to characterize vegetation and mitigate its influence on the passive microwave signal. Since snow contamination prevents the calculation of surface water, snow-covered pixels (as defined by meteorological re-analysis) are assigned a water fraction of 0 for the previous studies and in the distributed GIEMS-2 product. Passive microwaves are sensitive to the presence of water, including estuarine and offshore marine waters. To avoid misinterpretation of the data, coastal pixels were filtered out in the distributed GIEMS-2 product, leading to a possible underestimation of inundated surface extent in the coastal areas. Here we use an unfiltered version of GIEMS-2 in which coastal regions are not excluded, in order to improve the coastal cleaning process during the production of GIEMS-MC based on GLWDv2, as described in Sect. 3.

The Global Lakes and Wetlands Database version 2 (GLWDv2) (Lehner et al., 2025a, b) provides comprehensive global maps of aquatic ecosystems synthesized from a variety of ground- and satellite-based data products. GLWDv2 combines various data products to generate consolidated and harmonized static maps representative of the period 1990–2020. The GLWDv2 product contains 33 wetland and water body classes, which are listed in Table S1 in the Supplement. GLWDv2 represents the maximum extent of each of its 33 classes (in pixel fraction) at a resolution of 15 arcsec

(approximately 500 m at the Equator). For this study, the 33 GLWDv2 class maps were aggregated at $0.25^\circ \times 0.25^\circ$.

Rice cultivation varies seasonally according to cropping calendars, and their inundated cover can be confused with that of wetlands. The majority of global rice paddy maps are static representations, typically for a specific time period. A notable data source that gives insights into the seasonality of rice paddy at global scale is the MIRCA2000 dataset (Portmann et al., 2010b, a). MIRCA2000 provides data on irrigated and rainfed cultivated areas at a resolution of 5 arcmin for each month of a reference year (representative of circa 2000). The dataset integrates several data sources, including agricultural statistics such as cropping calendar and remote sensing data. This study uses both irrigated and rainfed rice data extracted from the MIRCA2000 dataset.

2.2 Ancillary and correction datasets (ERA5, ESA CCI)

The European Centre for Medium-range Weather Forecasts reanalysis (ECMWF-ERA5) (Hersbach et al., 2020; Copernicus Climate Change Service, 2019) is a state-of-the-art reanalysis for climate applications. It provides global climate and weather data spanning from 1940 to the present. ERA-5 uses assimilation techniques by integrating a wide diversity of observational data to deliver hourly estimates of multiple atmospheric, land, and oceanic variables at a resolution of 31 km. ERA5 can be downloaded at a resolution of $0.25^\circ \times 0.25^\circ$ from <https://cds.climate.copernicus.eu> (last access: 12 January 2023). In the GIEMS-2 and GIEMS-MC process, the area covered with snow in a pixel is derived from the ERA5 variables snow density and snow depth.

The European Space Agency (ESA) Climate Change Initiative (CCI) Land Cover dataset (Defourny et al., 2017; Harper et al., 2023) provides a classification of land cover features at a spatial resolution of 300 m for each year from 1992 to 2022. The dataset is derived from various satellite Earth observation data. According to the standards of the United Nations Land Cover Classification System (Di Gregorio and Jansen, 2005), it contains 22 land cover classes (Table S2), including 18 vegetation categories and urban, bare, water bodies, and snow/ice categories. The ESA CCI Land Cover dataset can be accessed via the ESA CCI Land Cover project website: <https://maps.elie.ucl.ac.be/CCI/viewer/download.php> (last access: 12 May 2023). Here, we aggregated a version to $0.25^\circ \times 0.25^\circ$, where the dominant class within each pixel is determined based on the highest fractional coverage.

2.3 Comparison dataset (WAD2M)

The Wetland Area and Dynamics for Methane Modeling (WAD2M) version 2.0 dataset (Zhang et al., 2021b, a) is a comprehensive global product designed to support methane modelling. It provides the fraction of wetland area, including peatlands, at a resolution of $0.25^\circ \times 0.25^\circ$ and at a monthly

time step for 2000–2020. The WAD2M dataset uses dynamic data from the Surface Water Microwave Product Series (SWAMPS) dataset (Jensen and McDonald, 2019), which provides a monthly inundation fraction at $0.25^\circ \times 0.25^\circ$. Similar to GIEMS-2, SWAMPS is derived mainly from passive microwave observations from SSM/I and SSMIS, but the methodology and ancillary data used differ between the two products (Schroeder et al., 2015; Prigent et al., 2020), resulting in important differences in some regions (Pham-Duc et al., 2017; Bernard et al., 2024b). The creation of WAD2M involved combining SWAMPS surface inundation time series with static datasets to distinguish between different wetland types. The static datasets used in WAD2M production are four peatland maps (NCSCD from Hugelius et al., 2013, CAWASAR from Widhalm et al., 2015, GLWDv1 from Lehner and Döll, 2004, and CIFOR from Gumbrecht et al., 2017), one inland open water map (GSW from Pekel et al., 2016), one coastal mask (MOD44W from Carroll et al., 2009), and a seasonal irrigated rice map (MIRCA2000 from Portmann et al., 2010b). These static layers allow the wetland fractions to be rescaled to include non-inundated wetlands (peatlands) and exclude non-wetland inundated areas (irrigated rice paddies and open waters).

3 Methods

3.1 Overview of the methodology

GIEMS-2 uses satellite passive microwave data, which are particularly responsive to the presence of water, to determine the fraction of inundated and saturated soil per pixel. However, modifications to the GIEMS-2 dataset are required in order to remove inundated or saturated areas that are not wetlands (e.g. rice paddies, lakes, rivers, reservoirs) and to add wetlands where the water table may be undetectable below ground level (e.g. some peatlands). As a consequence of the aforementioned remote sensing approach, the present study will first distinguish the inundated wetlands identified by GIEMS-2 and then add the unsaturated wetlands. In addition to GIEMS-2, the GLWDv2 dataset will be used.

The original GIEMS-2 product (Prigent et al., 2020) has been extended to 2020 (Bernard et al., 2024b), and a special version without coastal filtering is used here. In total, seven steps, described in the following subsections, are required to derive wetland maps from these data. The operations are made in terms of pixel fraction f on a regular grid of $0.25^\circ \times 0.25^\circ$. Multiplication by pixel area is then needed to derive wetland extent. A summary of the procedure is shown in Fig. 1, and the seven steps are described in detail in the following subsections.

3.1.1 Applying ocean mask

For consistency with GLWDv2, we here used the regional shapefiles of the HydroATLAS database (version 1.0; Linke

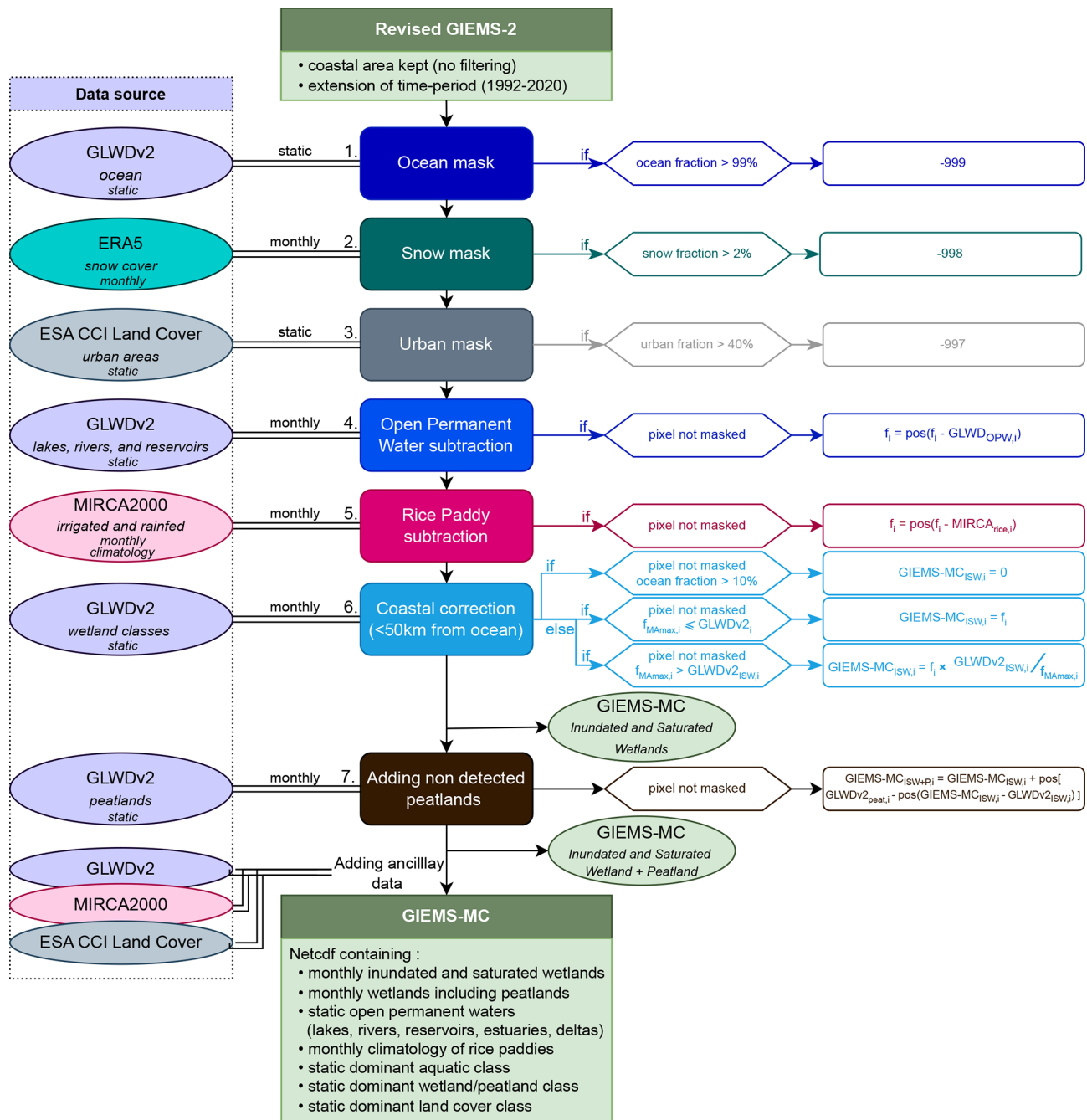


Figure 1. Schematic of the GIEMS-MC dataset production process. All operations are performed in terms of pixel fractions at a resolution of $0.25^\circ \times 0.25^\circ$. Ocean pixels are set to -999 , snow-covered pixels are set to -998 , and urban pixels are set to -997 in a revised version of GIEMS-2. Open permanent water and then rice paddies areas are subtracted from the surface water areas. A specific coastal cleaning is applied to remove ocean contamination, resulting in a dynamic map of inundated and saturated wetland ($\text{GIEMS-MC}_{\text{ISW}}$). Peatland areas undetected by GIEMS-2 are added to derive a dynamic map of all wetlands including peatlands, called inundated and saturated wetland + peatland ($\text{GIEMS-MC}_{\text{ISW+P}}$). Finally, initial ancillary data information is added to the product so that users can easily access the different fraction maps of all surface water categories, including inundated and saturated wetland, inundated and saturated wetland + peatland, open permanent waters, rice paddies, and the dominant wetland and vegetation classes. f_i refers to the fraction of a pixel i before the corresponding step. “pos” (f) refers to the positive part of f , i.e. $\text{pos}(f) = \max(f, 0)$. GLWDv2 open permanent water ($\text{GLWDv2}_{\text{OPW}}$) is the sum of all GLWDv2 classes 1 to 5 and 30. GLWDv2 inundated and saturated wetland ($\text{GLWDv2}_{\text{ISW}}$) is the sum of all GLWDv2 wetlands excluding peatlands corresponding to classes 8 to 21, 28, 29, 31, and 32. GLWDv2 peatland ($\text{GLWDv2}_{\text{peat}}$) is the sum of all GLWDv2 peatlands corresponding to classes 22 to 27.

et al., 2019), which provides near-identical coastlines as GLWDv2. This allowed us to calculate the ocean fraction for each $0.25^\circ \times 0.25^\circ$ pixel. The ocean water fraction is set to -999 if the ocean fraction of a pixel is greater than 99 %, to avoid confusion between ocean pixels and pixels where no surface water was detected (zero fraction pixels).

3.1.2 Applying snow mask

GIEMS-2 surface water detection relies primarily on passive microwave observations, which are affected by the presence of snow (Foster et al., 1984). Thus, the surface water fraction cannot be reliably quantified in the presence of snow. Consequently, the surface water detection algorithm in the GIEMS-2 production is not run when snow is present in a pixel. To exclude these snow-covered pixels, ECMWF snow information from ERA5 is used in the GIEMS-2 processing, and pixels with a snow fraction above 2 % are set to a surface water fraction of 0 (Prigent et al., 2020). In GIEMS-MC, the pixel value is given its dedicated snow flag value of -998 when the snow fraction of a pixel is greater than 2 %. It should be noted that this mask remains for all subsequent steps and is therefore also applied to the peatlands (step 7).

3.1.3 Applying urban mask

It has been observed that unexpectedly large water surfaces are detected by GIEMS-2 in areas of high urban density. This could be due to the different surface materials used in buildings, some of which strongly reflect microwaves. For example, highly reflective areas over Paris are misinterpreted as water due to predominance of zinc roofs. To apply an urban mask, the urban class product of the ESA CCI land cover map aggregated at $0.25^\circ \times 0.25^\circ$ is used. The grid cells with urban percentage above 40 % are systematically masked to -997 to avoid any confusion between urban and water surfaces. Note that applying this urban mask results in neglecting change in terms of surface water global area (< 1 % change on mean extent), but this avoids local artifacts over the high-urban density areas.

3.1.4 Subtracting open permanent waters

Inland open permanent waters are considered separately from wetlands in methane budgets (Saunois et al., 2020; Canadell et al., 2021), as different methane production and transport processes are involved. To derive wetland maps, these open permanent surface water areas must be subtracted from the GIEMS-2 estimates. Here, we define open permanent water as non-vegetated, permanently inundated areas that are not wetland. Some dynamic datasets could have been used, but consistency was preferred, so GLWDv2 harmonized maps were used in GIEMS-MC production. Then, open permanent water areas of GLWDv2 corresponding to layers 1 to 5 and 30 (freshwater lake, salt lake, reservoir, large river,

large estuarine river, and large river delta) are subtracted from the GIEMS-2 fractions. These GLWDv2 areas are derived from HydroLAKES (Messenger et al., 2016; lakes), the Global Dam Watch (GDWv1) database (Lehner et al., 2024; reservoirs), and the Global River Width from the Landsat (GRWL) dataset (Allen and Pavelsky, 2018; large rivers) and augmented with the Global Surface Water (GSW) database (Pekel et al., 2016). Note that the floodplain ecosystems are included in other GLWDv2 classes (10 to 15) and are therefore retained in GIEMS-2 when constructing GIEMS-MC.

3.1.5 Subtracting rice paddies

Rice paddies are intermittently saturated or inundated depending on irrigation practices, and their methane emissions are considered to be an anthropogenic source that should be separated from those of natural wetlands. GLWDv2 contains a static rice paddy map, but the seasonal variation of rice paddies is important in terms of extent and needs to be taken into account to avoid over-subtraction of rice paddies in the GIEMS-MC process. However, there is to our knowledge no dynamic (intra-annual resolution) product available that represents rice paddies at global scale over our observation period. As the MIRCA2000 product provides maps with a typical seasonality (circa 2000) of global rice paddies, it appears to be the most appropriate product available. Consequently, the MIRCA2000 12-month seasonality of irrigated and rain-fed rice paddy areas is subtracted from the area estimates. This rice paddy processing and its uncertainties are discussed further in Sect. 5.2.2.

3.1.6 Correcting ocean contamination

The GIEMS-2 version used here has not been filtered in coastal areas, as it is usually done in the distributed GIEMS-2 version. The SSM/I and SSMIS passive microwave observations used in GIEMS-2 production are very sensitive to the presence of water, including the ocean. The GIEMS-2 fraction and seasonality estimates are less reliable for pixels with larger ocean fractions. Thus, pixels containing more than 10 % ocean in GLWDv2 ($\text{GLWDv2}_{\text{ocean}} > 10\%$) are set to 0. Tests were made to tune this 10 % threshold, to avoid masking all pixels containing a small fraction of ocean area while ensuring reasonable seasonality. However, pixels containing up to 10 % ocean area will undergo an additional coastal cleaning procedure that follows. Ocean contamination can arise not only from the presence of ocean within the pixel but also from the ocean in neighbouring pixels. A GIEMS-2 pixel ($\sim 800 \text{ km}^2$ at the Equator, $\sim 400 \text{ km}^2$ at 60° N or S) is smaller than the -3 dB footprint of the original microwave satellite observations ($69 \text{ km} \times 43 \text{ km}$ at 19 GHz and $37 \text{ km} \times 28 \text{ km}$ at 37 GHz). Moreover, microwave energy is also measured in the side lobes of the satellite instrument footprint. Coastal areas should then undergo a cleaning process to reduce these artifacts. Pixels whose centres

are between 0 and 50 km from a coastline or large lakes ($> 15\,000\text{ km}^2$) are considered coastal areas.

In an attempt to correct for ocean contamination, the following procedure is applied to ensure that the wetland areas in GIEMS-MC in coastal regions are equal to or lower than the GLWDv2 inventory. This is done by calculating GLWDv2 inundated and saturated wetland ($\text{GLWDv2}_{\text{ISW}}$), i.e. the sum of all GLWDv2 wetlands excluding peatlands (which are not necessarily saturated surface water) corresponding to classes 8 to 21, 28, 29, 31, and 32. The fraction of the modified version of GIEMS-2 up to this step, incorporating the five aforementioned corrections and cleaning processes (ocean, snow, urban masks and open water, and rice paddies removal), is called f . Its mean annual maximum f_{MAmax} is calculated by taking a monthly average over all years and taking the maximum of this monthly seasonality for each pixel i . In the coastal region, for each time step and for each pixel i , with the resulting areas called the inundated and saturated wetland map in GIEMS-MC ($\text{GIEMS-MC}_{\text{ISW}}$):

- If $\text{GLWDv2}_{\text{ocean}, i} > 10\%$, then $\text{GIEMS-MC}_{\text{ISW}, i} = 0$.
- If $\text{GLWDv2}_{\text{ocean}, i} \leq 10\%$ and $f_{\text{MAmax}, i} < \text{GLWDv2}_{\text{ISW}, i}$, then $\text{GIEMS-MC}_{\text{ISW}, i} = f_i$.
- If $\text{GLWDv2}_{\text{ocean}, i} \leq 10\%$ and $f_{\text{MAmax}, i} > \text{GLWDv2}_{\text{ISW}, i}$, then $\text{GIEMS-MC}_{\text{ISW}, i} = f_i \cdot \frac{\text{GLWDv2}_{\text{ISW}, i}}{f_{\text{MAmax}, i}}$.

3.1.7 Adding peatlands

Finally, in order to have a complete map of wetlands, the peatlands not detected by GIEMS-2 (monthly unsaturated or unflooded peatlands) have to be taken into account in the wetland fraction. This is done using the following procedure. The sum of GLWDv2 peatlands, i.e. GLWDv2 classes 22 to 27, is denoted here as $\text{GLWDv2}_{\text{peat}}$. GLWDv2 peatland information is a composite product relying on the most up-to-date peatland maps: PeatMap (Xu et al., 2018, global), Soil-Grids250m (Hengl et al., 2017, global), NCSCD (Hugelius et al., 2013, north of 23°N), and CIFOR (Gumbricht et al., 2017, only south of 23.5°N). More details can be found in Lehner et al. (2025a). $\text{GLWDv2}_{\text{peat}}$ represents 4.26 Mkm^2 , which is consistent with primary PeatMap estimates of 4.23 Mkm^2 . The peatlands detected by GIEMS-2 are derived by the difference, if positive, between $\text{GIEMS-MC}_{\text{ISW}}$ and $\text{GLWDv2}_{\text{ISW}}$. The undetected peatlands are then derived for each month as the difference between $\text{GLWDv2}_{\text{peat}}$ and the peatlands detected by GIEMS-2. These undetected peatlands are added to $\text{GIEMS-MC}_{\text{ISW}}$, resulting in GIEMS-MC inundated and saturated wetland + peatland ($\text{GIEMS-MC}_{\text{ISW+P}}$).

That is, for each pixel i ,

$$\begin{aligned} \text{undetected_peatlands}_i &= \text{pos}[\text{GLWDv2}_{\text{peat}_i} \\ &\quad - \text{pos}(\text{GIEMS-MC}_{\text{ISW}_i} - \text{GLWDv2}_{\text{ISW}_i})] \\ \text{GIEMS-MC}_{\text{ISW+P}} &= \text{GIEMS-MC}_{\text{ISW}} \\ &\quad + \text{undetected_peatlands}. \end{aligned} \quad (1)$$

The uncertainty in terms of areas of this step is discussed in Sect. 5.2.3.

3.2 Comparison

$\text{GIEMS-MC}_{\text{ISW}}$ is compared with the original GIEMS-2 product and GLWD_{ISW} . $\text{GIEMS-MC}_{\text{ISW+P}}$ is compared to $\text{GLWDv2}_{\text{ISW+P}}$ ($\text{GLWDv2}_{\text{ISW}} + \text{GLWDv2}_{\text{peat}}$) and to WAD2M, as all also include peatlands (Table 3, Fig. 2, and Fig. S1). As GLWDv2 is a static map representing long-term maximum extent, the GIEMS-MC long-term maximum (LTmax) will be used for comparison with GLWDv2 instead of MAMax (Table 3). To derive this LTmax, the maximum of each pixel over the whole time period is selected. This can lead to the selection of extreme values with moderate reliability, and LTmax should then be interpreted with caution.

3.3 Description of GIEMS-MC dataset

Following the seven steps outlined, a NetCDF product at $0.25^\circ \times 0.25^\circ$ resolution containing the derived variables and ancillary variables is created. The variables included in this product are detailed in Table 1. Its components include both dynamic monthly maps of $\text{GIEMS-MC}_{\text{ISW}}$ and $\text{GIEMS-MC}_{\text{ISW+P}}$. Open permanent water classes (GLWDv2), i.e. freshwater lake, saline lake, reservoir, river, large estuarine river, and large river delta, are also added as static variables in GIEMS-MC. The 12-month seasonality of irrigated and rainfed rice paddy (MIRCA2000) is included. Three static maps provide information on the main ecosystems per pixel: the dominant aquatic class (GLWDv2), the dominant wetland or peatland class (GLWDv2), and the dominant land cover class (ESA CCI Land Cover map). This vegetation information is added in GIEMS-MC as it is expected to help improve the estimation of wetland methane emissions (Pangala et al., 2017; Vroom et al., 2022; Feron et al., 2024; Girkin et al., 2025; Ge et al., 2024).

4 GIEMS-MC results

4.1 Global inland water areas

To quantify the variations in terms of extent, the mean annual maximum (MAMax), mean annual mean (MAmean), and mean annual minimum (MAmin) are calculated by averaging the 29 years of data (21 years for WAD2M) to a typical 12-month seasonality for each pixel. Then, the maximum, the mean, and the minimum are respectively selected for each

pixel. Spatial correlation is defined as the pixel-by-pixel correlation between two maps, considering a specific unmasked region.

Globally, GIEMS-MC_{ISW} represents 3.80 Mkm², with a MAmean of 1.23 Mkm² (Table 2). The addition of peatlands greatly increases these global areas, with GIEMS-MC_{ISW+P} reaching 7.75 Mkm² (+3.95 Mkm²) in terms of MAMax and 3.54 Mkm² (+2.27 Mkm²) in terms of MAmean. This increase is mainly due to Europe–Siberia and North America, where large peatlands contribute significantly to the total wetland area (74 % and 58 % respectively).

GIEMS-MC_{ISW} consistently shows a much lower extent than the original GIEMS-2 (MAMax reduced from 6.80 to 3.80 Mkm²) that comprises all inundated and saturated areas, including non-wetland categories. The lower areas in GIEMS-MC_{ISW} are mainly due to the removal of open permanent waters in Europe, Siberia, and North America and to rice paddy subtraction in Asia. The LTmax of GIEMS-MC_{ISW} reaches 8.77 Mkm², close to the GLWDv2_{ISW} estimates of 8.22 Mkm².

Globally, the MAmean estimates of GIEMS-MC_{ISW+P} and WAD2M are in agreement (MAmean of 3.50 and 4.21 Mkm², respectively), and the two datasets show a spatial correlation coefficient of 0.61 for MAMax over submerged land. However, regional differences exist in Africa (MAmean of 295 and 719 × 10³ km², respectively) and Oceania (MAmean of 429 and 572 × 10³ km², respectively). In those regions, WAD2M detects comparatively more water, likely due to desert contamination in the SWAMPS product used in the WAD2M production (see Figs. 2 and S1). In Asia, Europe, Siberia, and North America, GIEMS-MC_{ISW+P} shows similar MAmean areas but has a larger MAMax–MAmin amplitude, possibly due to (1) higher peatland estimates in GLWDv2 than in the ancillary data used in WAD2M production, which could explain the higher MAMax, and (2) more stringent snow and coastal filtering in GIEMS-MC, which could explain the lower MAmin. As GLWDv2 peatlands are used to derive GIEMS-MC_{ISW+P} from GIEMS-MC_{ISW}, similar total extents are consistently found between the GIEMS-MC_{ISW+P} LTmax of 12.25 Mkm² and the GLWDv2_{ISW+P} LTmax of 12.49 Mkm².

Figure 3 provides the latitudinal distribution of (a) GIEMS-MC variables and (b) GIEMS-MC_{ISW+P} against WAD2M. GIEMS-MC_{ISW} shows a relatively uniform distribution across all latitudinal zones, with a peak just south of the Equator due to the Amazon basin. The inclusion of peatlands in GIEMS-MC_{ISW+P} increases largely the wetland area in the boreal (> 55° N; e.g. the Hudson Bay and the Siberian Lowland) and tropical (10° S–5° N; e.g. the Congo Basin) bands, leading to a similar distribution in WAD2M (Figs. 2 and 3c). Differences between GIEMS-MC_{ISW+P} and WAD2M are observed around 15° N and 10–30° S, due to discrepancies between the SWAMPS and GIEMS-2 methodologies (Pham-Duc et al., 2017; Bernard

Table 1. Summary of GIEMS-MC variables with corresponding data sources and temporal resolution. For details about data sources, see Sect. 2 or Prigent et al. (2020) for GIEMS-2, Lehner et al. (2025a) for GLWDv2, Portmann et al. (2010b) for MIRCA2000, and Defourny et al. (2017) for ESA CCI Land Cover.

GIEMS-MC variable	Long name	Type	Primary or main data source	Time resolution
inund_sat_wetland_frac	inundated and saturated wetland	fraction	GIEMS-2	monthly
inund_sat_peat_wetland_frac	inundated and saturated wetland + peatland	fraction	GIEMS-2 + GLWDv2	monthly
fresh_lake_frac	freshwater lake	fraction	GLWDv2	static
saline_lake_frac	saline lake	fraction	GLWDv2	static
reservoir_frac	reservoir	fraction	GLWDv2	static
river_frac	large river	fraction	GLWDv2	static
estu_river_frac	large estuarine river	fraction	GLWDv2	static
delta_frac	large river delta	fraction	GLWDv2	static
rice_irri_frac	irrigated rice paddy	fraction	MIRCA2000	12-month seasonality
rice_rainfed_frac	rainfed rice paddy	fraction	MIRCA2000	12-month seasonality
dom_aqua_class	dominant aquatic class	33 classes (Table S1)	GLWDv2	static
dom_wet_peat_class	dominant wetland or peatland class	25 classes (Table S1)	GLWDv2	static
dom_land_cover_class	dominant land cover class	37 classes (Table S2)	ESA CCI Land Cover	static

Table 2. Global and continental surfaces of GIEMS-MC variables in 10^3 km^2 . For dynamic classes, MAm_{ax} and MAm_{in} are shown. Total MAm_{ax} is the sum of GIEMS-MC inundated and saturated wetland + peatland MAm_{ax}, open permanent water (freshwater lake, saline lake, reservoir, river, large estuarine river, large river delta) from GLWDv2, and rice paddy from MIRCA2000 MAm_{ax} (irrigated and rainfed). Regions correspond to the shapefiles of HydroATLAS database (version 1.0; Linke et al., 2019).

		Global	Africa	Asia	Europe + Siberia	Oceania	North America	South America
GIEMS-MC _{ISW} (inundated and saturated wetland)	MAm _{ax}	3796	515	972	616	207	827	207
	MAm _{ean}	1227	163	252	154	103	258	294
	MAm _{in}	251	46	29	11	46	30	85
GIEMS-MC _{ISW+P} (inundated and saturated wetland + peatland)	MAm _{ax}	7745	636	1153	2369	522	1985	1001
	MAm _{ean}	3500	295	382	888	429	790	654
	MAm _{in}	1308	182	96	79	377	76	449
Freshwater lake	static	2045	197	76	429	22	1214	81
Saline lake	static	359	33	97	88	40	21	20
Reservoir	static	316	40	62	71	6	87	47
River	static	384	40	72	109	13	53	93
Large estuarine river	static	79	5	12	16	9	10	13
Large river delta	static	280	18	139	15	0	35	57
Irrigated rice paddy	MAm _{ax}	639	14	509	16	46	14	22
	MAm _{ean}	431	8	355	6	30	8	10
	MAm _{in}	64	0	62	0	0	0	0
Rainfed rice paddy	MAm _{ax}	614	42	452	0	71	3	25
	MAm _{ean}	251	21	178	0	29	1	12
	MAm _{in}	1	0	0	0	0	0	0
Total	MAm _{ax}	12271	1013	2495	3102	731	3400	1326
Total distribution	MAm _{ax}	100 %	8.3 %	20.3 %	25.3 %	6.0 %	27.7 %	10.8 %

et al., 2024b), mostly related to desert contamination in SWAMPS (the Sahel and Australia in Fig. 2).

4.2 Regional spatial patterns over main basins

GIEMS-MC_{ISW} and GIEMS-MC_{ISW+P} data are analysed in the following sections over large wetland complexes representing different environments: the Siberian Lowland, the Sudd, the Amazon, and South-East Asia.

As expected, peatland addition noticeably amplifies the extent between GIEMS-MC_{ISW} (MAm_{ax} of 0.19 Mkm^2) and GIEMS-MC_{ISW+P} (MAm_{ax} of 0.70 Mkm^2) over the Ob basin (Western Siberian Lowland; Fig. 4). WAD2M and GIEMS-MC_{ISW+P} consistently present similar patterns for MAm_{ax} (spatial correlation coefficient of 0.80). However, discrepancies occur in the southern part of the Ob basin that can be attributed to different snow filtering between SWAMPS (used for WAD2M) and GIEMS-2 (used for GIEMS-MC). The Boreal–Arctic Wetland and Lake Dataset (BAWLD) is also shown for comparison (Fig. 4), as it covers the upper part of the basin (Olefeldt et al., 2021b, a). The BAWLD wetland fraction, including peatland classes,

exhibits patterns similar to GIEMS-MC_{ISW+P} MAm_{ax}, with a spatial correlation coefficient of 0.74. BAWLD covers a slightly larger area (+6 %) compared to GIEMS-MC_{ISW+P} MAm_{ax} when comparing the common area covered by the two datasets.

In the Sudd basin shown in Fig. 5, GIEMS-MC_{ISW+P} extent corresponds essentially to GIEMS-MC_{ISW}, indicating minimal presence of peatlands. For comparison, two surface water extent products, both derived from Cyclone Global Navigation Satellite System L-band remote sensing observations, are also shown (Zeiger et al., 2023; Zeiger, 2023; Gerlein-Safdi and Ruf, 2021; Gerlein-Safdi et al., 2021). Gerlein-Safdi and Ruf (2021) estimates are available for the southern part of the basin (MAm_{ax} of 0.27 Mkm^2 for 2018–2019) and are much higher than the GIEMS-MC (MAm_{ax} of 0.04 Mkm^2 for 2018–2019) and WAD2M (MAm_{ax} of 0.1 Mkm^2 for 2018–2019) estimates. The Zeiger (2023) product provides an MAm_{ax} of 0.06 over August 2018 to July 2019, which is within the GIEMS-MC and WAD2M estimates. While good agreement is observed in the southern part of the basin between the spatial pattern of GIEMS-MC_{ISW+P}, WAD2M, and the product of Zeiger (2023), sig-

Table 3. Comparison of GIEMS-MC_{ISW} and GIEMS-MC_{ISW+P} surface extents with WAD2M (Zhang et al., 2021b) and GLWDv2 (Lehner et al., 2025a) datasets, in 10³ km². For dynamic classes, MAmax and MAmin are shown. GLWDv2_{ISW} refers to the sum of GLWDv2 classes 8 to 21, 28, 29, 31, and 32, while GLWDv2_{ISW+P} refers to the sum of GLWDv2 classes 8 to 29, 31, and 32. Regions correspond to the shapefiles of the HydroATLAS database (version 1.0; Linke et al., 2019).

		Global	Africa	Asia	Europe + Siberia	Oceania	North America	South America
GIEMS-MC _{ISW} (inundated and saturated wetland)	LTmax	8766	1409	2097	1548	648	1594	1465
	MAmax	3796	515	972	616	207	827	207
	MAmean	1227	163	252	154	103	258	294
	MAmin	251	46	29	11	46	30	85
Original GIEMS-2	MAmax	6796	631	1793	1071	339	1804	945
	MAmean	2730	236	659	339	216	647	506
	MAmin	795	88	149	42	133	93	218
GLWDv2 _{ISW} (inundated and saturated wetland)	static	8223	1010	1958	1416	541	1755	1269
GIEMS-MC _{ISW+P} (inundated and saturated wetland + peatland)	LTmax	12 251	1512	2242	3115	915	2628	1760
	MAmax	7745	636	1153	2369	522	1985	1001
	MAmean	3500	295	382	888	429	790	654
	MAmin	1308	182	96	79	377	76	449
WAD2M	MAmax	6756	1077	743	1675	678	1308	985
	MAmean	4208	719	370	776	572	760	778
	MAmin	2437	479	184	176	482	293	639
GLWDv2 _{ISW+P} (inundated and saturated wetland + peatland)	static	12 486	1147	2156	3280	878	3023	1646

nificant disparities emerge between WAD2M and the two products in the north-eastern desert region of the Sudd basin, probably due to contamination in the original SWAMPS dataset.

Over the Amazon (Fig. 6), GIEMS-MC_{ISW} fractions are high (> 0.5) along the main river channel, while including peatlands adds smaller surfaces along smaller secondary channels, resulting in finer spatial patterns and higher MAmax (0.31 to 0.56 Mkm²). The resulting GIEMS-MC_{ISW+P} MAmax map closely resembles that of WAD2M (spatial correlation coefficient of 0.77), with a slightly higher MAmax for WAD2M (0.47 Mkm²). GIEMS-MC_{ISW} and GIEMS-MC_{ISW+P} extents can be potentially underestimated in this basin, as Fleischmann et al. (2022) found that GIEMS-2 estimates of inundation were likely slightly underestimated compared to higher-resolution remote sensing estimates based on synthetic aperture radar (SAR), with Chapman et al. (2015) finding +4 % and Rosenqvist et al. (2020) +36 % compared to GIEMS-2 long-term maximum inundation.

GIEMS-MC_{ISW+P} and WAD2M agree well in South-East Asia (Fig. 7, with a MAmax spatial correlation coefficient of 0.67), with GIEMS-MC_{ISW+P} showing greater peatland extent than WAD2M due to higher peatland areas estimated by GLWDv2 used in GIEMS-MC production than the earlier estimates used in WAD2M.

These findings underline the legacy of the two original microwave-based datasets (GIEMS-2 and SWAMPS) used respectively in GIEMS-MC and WAD2M production, despite the corrections. Indeed, methodological disparities between GIEMS-2 and SWAMPS production may lead to distinct spatial inundation detection patterns, particularly in regions where contamination from ocean, desert, and snow needs careful consideration.

4.3 Temporal seasonal and inter-annual variations

The temporal dynamics of GIEMS-2 were extensively examined in Prigent et al. (2020) and evaluated in Bernard et al. (2024b), where it was compared with other hydrological observations, including MODIS-derived surface water extent (Frappart et al., 2018; Normandin et al., 2018, 2024), CYGNSS-derived (Zeiger et al., 2023) surface water extent, and river discharge. The evaluation showed that GIEMS-2 reliably captures temporal variations, including seasonality and inter-annual variabilities, even in regions with dense vegetation cover (Figs. 8 and 9).

4.3.1 Seasonal variations

The 2000–2020 mean seasonality of GIEMS-MC_{ISW}, GIEMS-MC_{ISW+P}, and WAD2M over the Ob, the Sudd,

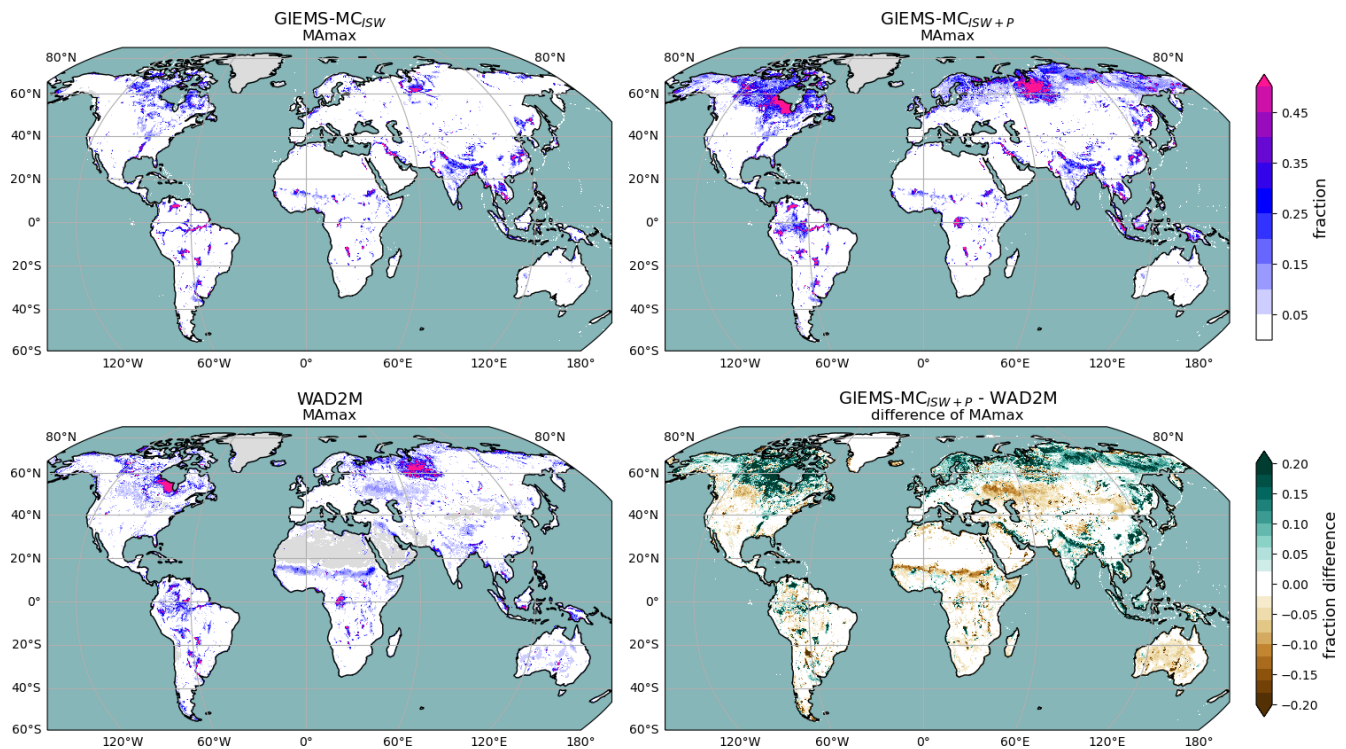


Figure 2. Global distribution of the MMax of GIEMS-MC_{ISW}, GIEMS-MC_{ISW+P}, and WAD2M (Zhang et al., 2021b), as well as the difference in MMax from GIEMS-MC_{ISW+P} and WAD2M. Refer to Fig. S1 for maps with MMin.

the Amazon, and the Congo basins and South-East Asia are presented in Fig. 8 (left). The seasonal variations of the GIEMS-MC variables are driven by the dynamics of saturated and inundated wetlands (GIEMS-MC_{ISW}), with peatlands contributing to an offset effect between GIEMS-MC_{ISW} and GIEMS-MC_{ISW+P}. In the Ob, the Amazon, and the Congo basins and South-East Asia, GIEMS-MC_{ISW+P} exhibits comparable magnitudes to WAD2M. In the Sudd region, WAD2M shows distinct seasonality to GIEMS-MC and the two CYGNSS-derived products, probably due to the SWAMPS artifacts in desert regions mentioned above.

Across latitudinal bands, the global seasonality of GIEMS-MC_{ISW} and GIEMS-MC_{ISW+P} is mainly driven by the boreal and temperate northern regions, due to snow cover changes (Fig. 9, left). However, notable differences in terms of seasonal cycle between GIEMS-MC_{ISW+P} and WAD2M exist over the middle to high latitudes. Indeed, larger peatland surfaces are included in GIEMS-MC than in WAD2M (higher amplitude), and the more widespread snow masking in GIEMS-MC in the temperate zone leads to a stronger seasonal cycle compared to WAD2M. The seasonal cycles over the tropics and the Southern Hemisphere are more similar between GIEMS-MC_{ISW+P} and WAD2M, but surface extents are larger in WAD2M, predominantly due to desert and ocean contamination in SWAMPS, as discussed in Sect. 4.1.

4.3.2 Inter-annual variations and trends

Figure 8 (right) shows the deseasonalized monthly anomalies of GIEMS-MC_{ISW}, GIEMS-MC_{ISW+P}, and WAD2M over different regions, while Fig. 9 (right) corresponds to latitudinal bands. The reference seasonality period subtracted is the 2000–2020 seasonal average. As expected, GIEMS-MC_{ISW} and GIEMS-MC_{ISW+P} have the same anomalies for latitudes below 30° N because the temporal dynamics come from the inundated and saturated wetlands, not from the static peatland map. For northern temperate and boreal areas, the snow cover also imposes a seasonality on peatlands, which explains larger anomalies in GIEMS-MC_{ISW+P} than in GIEMS-MC_{ISW}. For GIEMS-MC_{ISW+P} over the boreal region (55–90° N), a positive trend is detected over May and June ($+10 \times 10^3 \text{ km}^2 \text{ yr}^{-1}$) and September and October ($+24 \times 10^3 \text{ km}^2 \text{ yr}^{-1}$) months that can possibly be attributed to earlier snow melt and delayed snow cover arrival.

No long-term trends were found at regional scales in GIEMS-MC_{ISW}, except for South-East Asia, where a small positive trend was found ($+1.7 \times 10^3 \text{ km}^2 \text{ yr}^{-1}$, i.e. $\sim +50 \times 10^3 \text{ km}^2$ for 30 years). This is likely mostly due to the increasing trend in rice paddies, which is not taken into account because only the MIRCA2000 climatology is used, and new rice paddies over the years are then aliased to wetlands over time (see Sect.5.2.2).

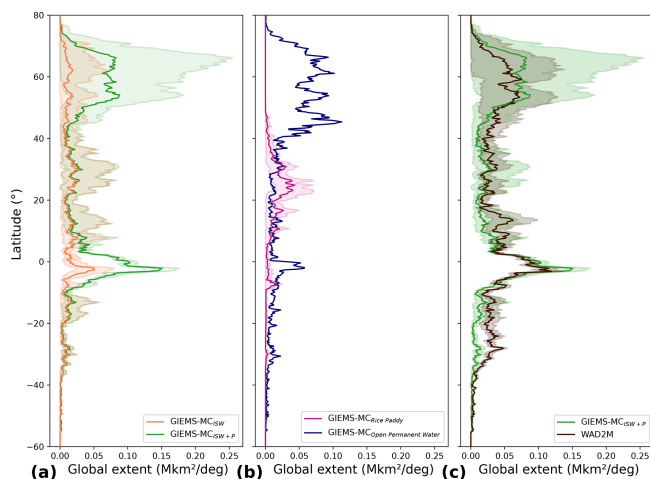


Figure 3. Latitudinal distributions of (a) the GIEMS-MC wetland variables (inundated and saturated wetlands, inundated and saturated wetlands + peatlands), (b) GIEMS-MC wetland ancillary variables (rice paddy, and the sum of open permanent water), and (c) GIEMS-MC_{ISW+P} and WAD2M products. For dynamic variables, solid lines represent the M_{Amean}, while coloured fillings represent the M_{Amax}–M_{Amin} interval. The extents are given per 1° latitudinal bin. The metrics (M_{Amin}, M_{Amean}, and M_{Amax}) are calculated over the entire product availability period, i.e. from 1992 to 2020 for the GIEMS-MC variables and from 2000 to 2020 for WAD2M.

An abrupt change in WAD2M inter-annual variability amplitude occurs over the Amazon and Congo basins in 2009, attributed to a change in one of the satellite data used in SWAMPS, together with a decreasing trend also found in the SWAMPS data (Fig. 8). Due to these problems in SWAMPS, the inter-annual variability of WAD2M should be considered with caution and makes time-series comparison with GIEMS-MC_{ISW+P} difficult over these regions.

5 Discussion

The production of GIEMS-MC involves seven steps, each of which not only contributes to the transition from inundation time series to wetland map time series, but also to the uncertainties of the final product. It has been estimated that the GIEMS product possibly underestimates surface water areas by less than 10 % (Prigent et al., 2007). This value can be used as an order of magnitude of the uncertainty in GIEMS-2, although methodological improvements have been made between GIEMS and GIEMS-2 (Prigent et al., 2020). This is also likely a realistic approximation for the GIEMS-MC_{ISW} error, as it uses mainly GIEMS-2 information. A quantification of the uncertainties of the GIEMS-MC variables would require a deeper knowledge of the measurement and detection uncertainties of all the products used, some of which are not calculated in the original source, which is beyond the scope of this study. However, it is possible to quantify the

influence of each step in the GIEMS-MC procedure and to study the sensitivity of the results to the processing choices.

5.1 Quantification of the influence of each process step on the GIEMS-MC global extents

Table 4 shows the influence of the successive steps in terms of M_{Amax}, M_{Amean}, and M_{Amin}. The removal of open permanent water (step 4) and the subtraction of rice paddies (step 5) have a significant impact on the global extent, both resulting in a subtraction of -2.34 Mkm^2 on M_{Amax} and -1.16 Mkm^2 on M_{Amean}. Coastal cleaning also has a large influence on the reduction of the area: -2.60 Mkm^2 in M_{Amax} and -1.60 Mkm^2 in M_{Amean} and especially on M_{Amin}, which decreases from 1.17 to 0.26 Mkm^2 . In fact, the coastal region has an artificially high minimum value due to ocean contamination before this cleaning step. Finally, the addition of peatlands turns out to be an extremely significant step in terms of surface area for GIEMS-MC_{ISW+P}, with large increases observed in both M_{Amax} ($+3.94 \text{ Mkm}^2$) and M_{Amean} ($+2.27 \text{ Mkm}^2$) extents.

5.2 Sensitivity to the GIEMS-MC procedure

The three critical stages in the production of GIEMS-MC are further discussed in this section, along with the use of a snow mask.

5.2.1 Coastal processing

In the methods in Sect. 3.1.6, we chose to apply a cleaning procedure to coastal pixels located within 50 km of the coast. Figure 10a shows the global mean seasonality of GIEMS-MC_{ISW} and GIEMS-MC_{ISW+P} when considering coastal bands ranging between 0 and 100 km from the coast to be processed using GLWDv2 information, following the methodology in Sect. 3. After removing the pixels with more than 10 % ocean, the cleaning of the coastal band up to 30 km from the coast reduces GIEMS-MC_{ISW} M_{Amax} by 0.7 Mkm^2 . Cleaning also the 30–50 km band reduces it further by 0.5 Mkm^2 , while the 50–70 km (-0.12 Mkm^2) and 70–100 km (-0.08 Mkm^2) bands have smaller effects. The cleaning over 50 km is consistent with our technical understanding of the contamination.

5.2.2 Rice subtraction

An issue concerning rice in GIEMS-MC production stems from the classification used in the MIRCA2000 dataset, which separates rice paddies into irrigated and rainfed types. Irrigated paddies are typically fully inundated at least part of the year. Rainfed paddies have variable levels of submergence, with approximately 80 % inundated and 20 % remaining upland paddies (Maclean et al., 2013). Under these conditions, the upland rice (9 % of total rice paddies area; Maclean et al., 2013) should not be subtracted from GIEMS-2 in the

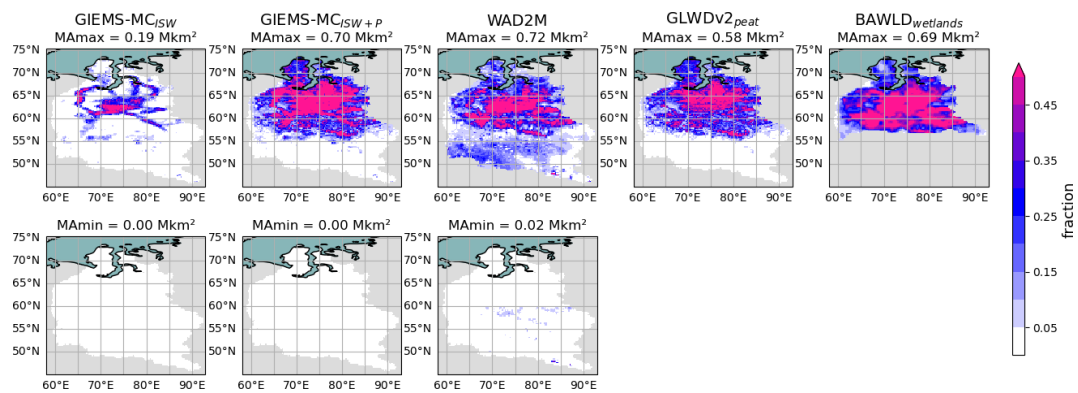


Figure 4. MAMax and MAmin maps of GIEMS-MC_{ISW} (1992 to 2020), GIEMS-MC_{ISW+P} (1992 to 2020), and WAD2M (2000 to 2020) over the Ob, as well as GLWDv2 peatland (static) and BAWLD wetland (static) maps. Low MAmin values are due to the snow mask.

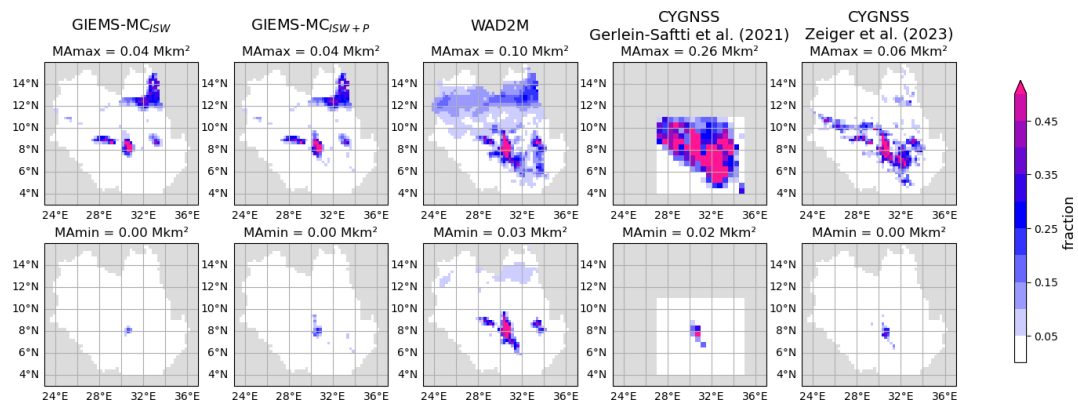


Figure 5. MAMax and MAmin maps over the Sudd region of GIEMS-MC_{ISW}, GIEMS-MC_{ISW+P} (1992 to 2020), and WAD2M (2000 to 2020) and CYGNSS-based estimates from Gerlein-Safti et al. (2021) (June 2017 to April 2020) and Zeiger et al. (2023) (August 2018 to July 2020). The available periods differ between the products.

GIEMS-MC processing steps if we could distinguish upland rice from the rest of the rainfed paddies. To explore this, we attempted a classification based on topographic information to separate inundated from non-inundated within the rainfed rice category. The resulting maps, shown in Table S3, lead to surface extent inconsistent with FAO statistics per country (FAO, 2002). In the absence of any reliable distinction possibility, the total rice paddies were subtracted, acknowledging that the subtracted area might be overestimated by about 9 %. Note that this light overestimation of subtracted rice paddies might be counterbalanced by the fact that MIRCA2000 areas estimates are underestimated when compared to FAOSTAT (Fig. 11).

In WAD2M production, the MIRCA2000 is also used to differentiate rice paddies from wetlands, but only irrigated paddy class is subtracted (Zhang et al., 2021b). To evaluate the impact of rice handling in GIEMS-MC, Fig. 10b shows global seasonality of GIEMS-MC_{ISW} and GIEMS-MC_{ISW+P} if only irrigated rice paddies are subtracted or if both irrigated and rainfed are subtracted. The difference occurs mainly between June and October, in the Northern Hemisphere sum-

mer, corresponding to a difference of 0.25 Mkm² in terms of MAMax (6 % of GIEMS-MC_{ISW} and 3 % GIEMS-MC_{ISW+P} MAMax). While this has a moderate influence on global extent, this difference can be important in rice-cultivating countries, e.g. a difference of 30 % in GIEMS-MC_{ISW} MAMax over India depending on the type of subtraction used. For GIEMS-MC_{ISW+P}, as the total surfaces are higher, the influence of rice paddy subtraction is proportionally less important.

Finally, subtracting the MIRCA2000 climatology in the GIEMS-MC processing and not taking into account the inter-annual variation of rice paddies and their inter-annual changes in inundation over the period 1992–2020 can lead to misclassification of rice paddies as wetlands. First, rainfed rice paddies in particular show significant inter-annual changes in inundation. Furthermore, the surface covered by rice paddies also changes over the years. The MIRCA2000 product is compared in Fig. 11 with the estimates from the Food and Agriculture Organization (FAO) of the United Nations FAOSTAT (<https://www.fao.org/faostat/en/#data/QCL>, last access: 30 June 2023). FAOSTAT is widely used for

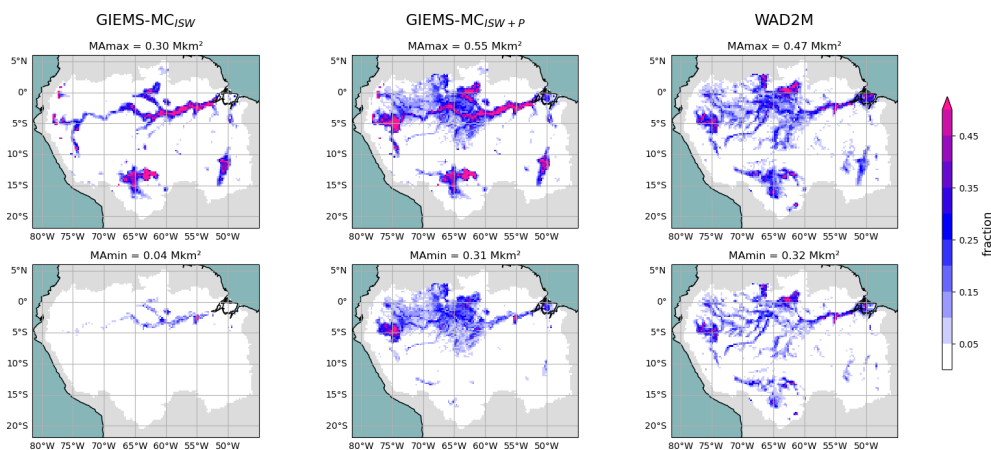


Figure 6. MMax and MAmin maps of GIEMS-MC_{ISW} (1992 to 2020), GIEMS-MC_{ISW}+P (1992 to 2020), and WAD2M (2000 to 2020) over the Amazon basin.

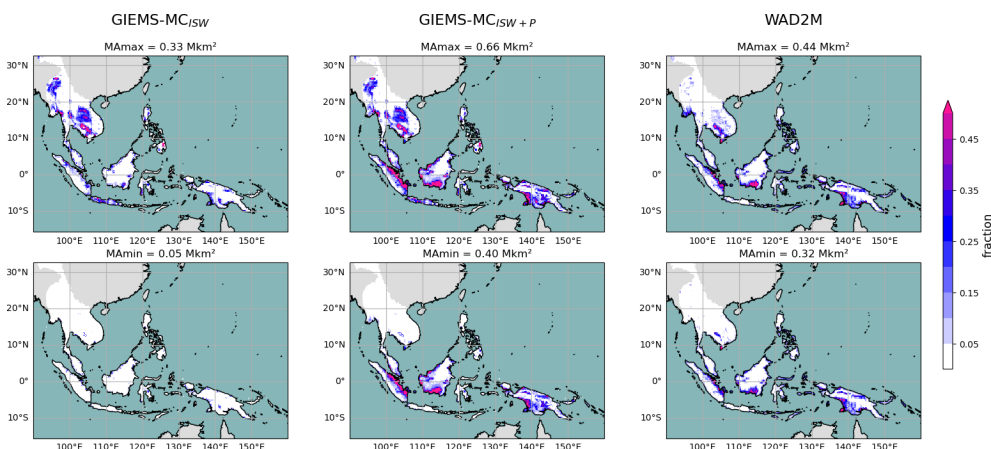


Figure 7. MMax and MAmin maps of GIEMS-MC_{ISW} (1992 to 2020), GIEMS-MC_{ISW}+P (1992 to 2020), and WAD2M (2000 to 2020) over South-East Asia.

global estimates of methane emissions from rice paddies, notably in the Emissions Database for Global Atmospheric Research (EDGAR; Janssens-Maenhout et al., 2019). The cropland area of rice paddies is increasing in South-East Asia, with FAOSTAT estimating $+60 \times 10^3 \text{ km}^2$ between 1992 and 2020 in this region, which corresponds to the increasing trend of $\sim +50 \times 10^3 \text{ km}^2$ in GIEMS-MC_{ISW} over this period (Sect. 4.3.2).

MIRCA2000 (MMax of 1.25 Mkm^2) presents smaller rice paddy extent than FAOSTAT (1.47 Mkm^2 in 1992 to 1.64 Mkm^2 in 2020). In GLWDv2, the map from Salmon et al. (2015) is used as primary information but undergoes numerous corrections related to artifacts in the product, including double-checking information using the RiceAtlas (Laborte et al., 2017). This led to a static map of rice paddies of 1.2 Mkm^2 , close to MIRCA2000 MMax estimates. Then, various inventories of anthropogenic methane emissions that account for rice methane emissions do not use the same maps for rice paddies, which can lead to mismatches

across the estimates (surfaces double counting or miscounting). Efforts to use similar compatible rice maps between the two research communities would greatly improve the consistency of wetland time series and then the methane emission estimates. A dynamic map that accurately reflects the temporal variation of inundated rice paddies would better meet the needs of remote sensing wetland mapping. This approach would address the limitations of existing classifications, such as MIRCA's irrigated/rainfed or FAO's yearly irrigated/rainfed/upland categories, which do not adequately address the specific needs of the community.

5.2.3 Peatland integration

Peatlands contribute to more than half of areas in GIEMS-MC_{ISW}+P (Table 4) and depend highly on the GLWDv2 peatland map used here.

Most of the peatlands are not saturated or inundated areas, although some can have their water table above the peat

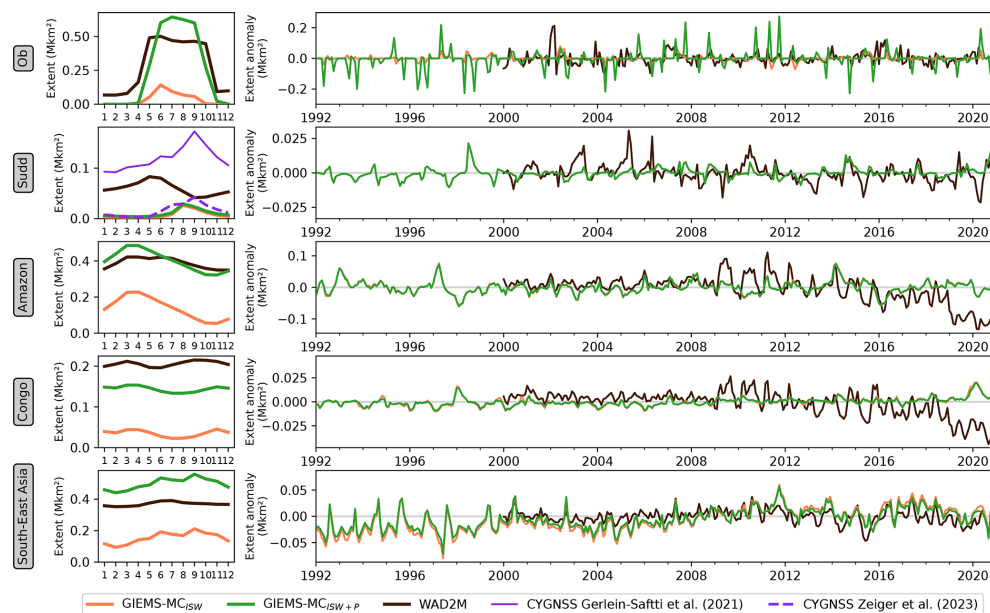


Figure 8. Left: monthly mean seasonal cycle of GIEMS-MC_{ISW}, GIEMS-MC_{ISW+P}, and WAD2M over different regions. Right: deseasonalized monthly anomalies of the same three variables. To derive the deseasonalized monthly anomalies, the average monthly seasonal cycle was subtracted from the long-term monthly time series. For the Sudd basin seasonality comparison, estimations from Gerlein-Safdi et al. (2021) (June 2017 to April 2020) and Zeiger et al. (2023) (August 2018 to July 2020) are added.

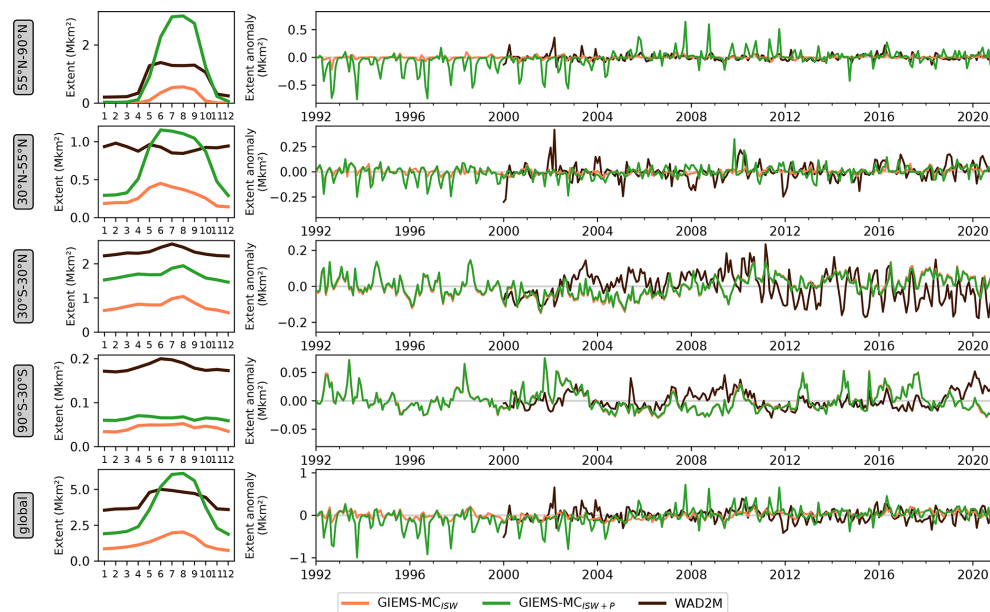


Figure 9. Left: monthly mean seasonal cycle of GIEMS-MC_{ISW}, GIEMS-MC_{ISW+P}, and WAD2M over different latitudinal bands. Right: deseasonalized monthly anomalies of the same three variables. To derive the deseasonalized monthly anomalies, the average monthly seasonal cycle was subtracted from the long-term monthly time series.

surface intermittently (Lourenco et al., 2023). A large part of peatlands are then not detected by GIEMS-2. Three ways of integrating GLWDv2 peatlands were tested to assess how sensitive the peatland integration method is. For each pixel i , we did the following:

1. Set GLWDv2_{peat} fraction as the minimum of GIEMS-MC_{ISW+P}, minimizing GIEMS-MC_{ISW+P} areas:
if $\text{GIEMS-MC}_{\text{ISW}_i} < \text{GLWDv2}_{\text{peat}_i}$, then $\text{GIEMS-MC}_{\text{ISW+P}_i} = \text{GLWDv2}_{\text{peat}_i}$.

Table 4. Global MAm_{ax}, MAm_{ean}, and MAm_{in} (in Mkm²) after each step of GIEMS-MC production. It should be noted that snow and oceans were already set to zero fraction in GIEMS-2 and that the snow mask is applied to all wetlands, including peatlands, and is then responsible for the low MAm_{in} values.

Step	Step description	MA _{max}	MA _{mean}	MA _{min}
0	GIEMS-2 revised version	9.02	4.15	1.63
1 to 3	After masking oceans, snow, and urban areas	8.83	4.03	1.58
4	After subtracting open permanent water	6.89	3.06	1.23
5	After subtracting rice paddies	6.30	2.77	1.12
6	After cleaning coasts (GIEMS-MC _{ISW})	3.80	1.23	0.25
7	After adding peatlands (GIEMS-MC _{ISW+P})	7.75	3.50	1.31

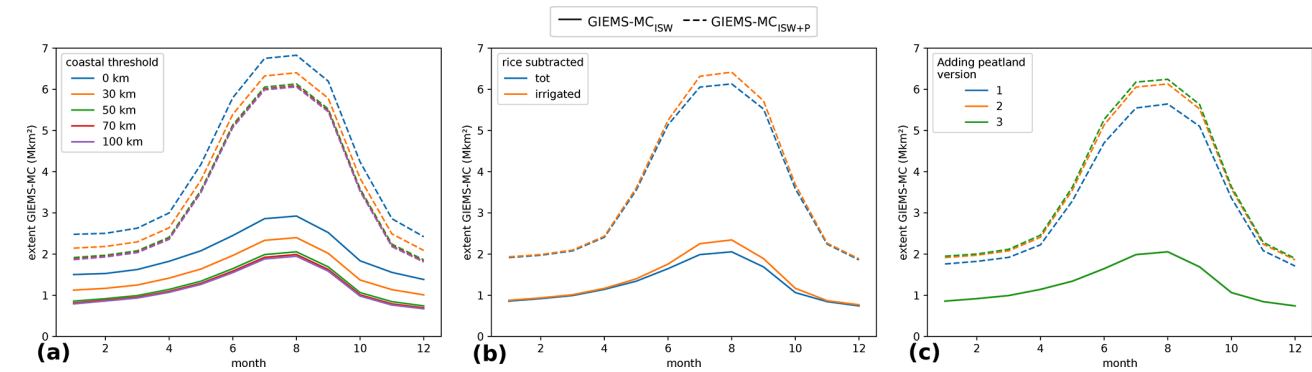


Figure 10. Sensitivity of GIEMS-MC averaged seasonality to the different steps of the production procedure: (a) the coastal threshold for coastal cleaning, (b) the rice procedure, and (c) the way peatlands are added. Solid lines represent the extent of GIEMS-MC_{ISW}, while dashed lines represent GIEMS-MC_{ISW+P}. Colours show the different GIEMS-MC treatments.

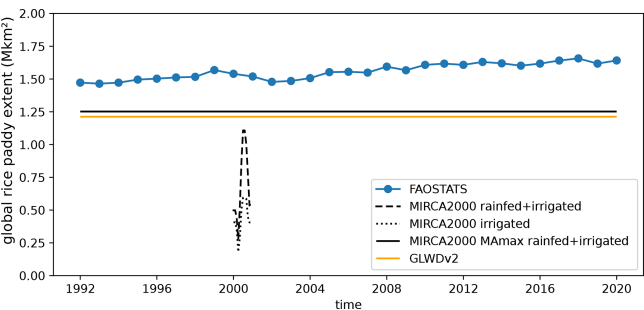


Figure 11. Rice paddy surface extent estimations from MIRCA2000 (Portmann et al., 2010b), FAOSTAT (<https://www.fao.org/faostat/en/#data/QCL>, last access: 30 June 2023), and GLWDv2 (Lehner et al., 2025a). MIRCA2000 MAm_{ax} is higher than the maximum of the MIRCA2000 seasonality plot because not all pixels have their maximum in the same month.

2. Attempt to add only the peatlands not detected by GIEMS-2 as described in the methods in Sect. 3.1.7:
$$\text{GIEMS-MC}_{\text{ISW}+P_i} = \text{GIEMS-MC}_{\text{ISW}_i} + \text{pos}[\text{GLWDv2}_{\text{peat}_i} - \text{pos}(\text{GIEMS-MC}_{\text{ISW}_i} - \text{GLWDv2}_{\text{ISW}+P_i})].$$
3. Add all GLWDv2 peatland, maximizing GIEMS-MC_{ISW+P} areas:

$$\text{GIEMS-MC}_{\text{ISW}+P_i} = \text{GIEMS-MC}_{\text{ISW}_i} + \text{GLWDv2}_{\text{peat}_i}.$$

The effects of these three peatland integration approaches on GIEMS-MC_{ISW+P} extent are represented in Fig. 10c. A difference of 0.85 Mkm² (11 %) is found for GIEMS-MC_{ISW+P} MAm_{ax} between the two extreme approaches 1 and 3. Approach 1 likely underestimates peatland integration, as some pixels can contain both inundated or saturated wetlands and peatlands. Approach 3 likely overestimates peatland integration, as some peatlands (inundated and saturated) should be detected in GIEMS-2. Method 2 appears as a sensible consensus, but this approach also likely overestimates peatland surfaces, as GLWDv2 wetland categories, used to discriminate detected and non-detected peatlands by GIEMS-2 (see Sect. 3.1.7), are a long-term maximum.

Non-inundated peatlands account for a significant proportion of the GIEMS-MC_{ISW+P} in terms of maximum area (50.2 % of the MAm_{ax}; see Table 2). The peatland map used in this study to derive GIEMS-MC_{ISW+P} comes from GLWDv2 and is a composite product based on four different estimates (see Sect. 3.1.7 or Lehner et al., 2025a). It should be emphasized that although this product is based on the best current knowledge, there is still limited consensus in the literature on the extent of peatlands. Mapping of peatlands remains challenging, as it is primarily a soil characteristic re-

lated to organic carbon content that cannot be directly detected by satellite data. Consequently, mapping efforts rely on approaches based on observations (in situ data and/or remote sensing proxies for, for example, vegetation or hydrological data) to map their extent using models or machine learning. This task is particularly difficult in tropical regions, where in situ data are sparse and where dense cloud cover and vegetation cover limit remote sensing observations; this results in fewer regional maps over the tropics, with frequent revisions towards higher estimates of tropical peatland areas (Dargie et al., 2017; Hastie et al., 2024).

5.2.4 Snow-covered pixel masking

Due to the influence of snow on passive microwave observations, snow-covered pixels are masked in the estimation of GIEMS-2 and GIEMS-MC inundation fractions (see Sect. 3.1.2). This masking prevents models from accounting for methane emissions from snow-covered areas. However, cold-season methane fluxes in arctic peatlands and tundra have been shown to contribute between 25 % and 50 % of the annual local fluxes (Bao et al., 2021; Ito et al., 2023; Mastepanov et al., 2008; Zona et al., 2016; Rößger et al., 2022). Therefore, the sensitivity of microwave remote sensing to snow is a limitation in boreal regions. Nevertheless, the boreal zones are estimated to contribute only about 5 % of annual global wetland and inland freshwater emissions using a top-down approach and about 10 % using a bottom-up approach (Saunois et al., 2025), with only up to half of these boreal emissions potentially occurring during the cold season. Consequently, the exclusion of snow-covered areas is likely to add only a few percent of uncertainty to global methane emissions from wetlands and inland waters.

For consistency with the snow mask used in GIEMS-2 production, we have used the same mask here in the GIEMS-MC generation. This mask is derived from the ERA5 product, which might overestimate the extent of snow cover but still captures interannual changes well (Kouki et al., 2023). The snow mask in GIEMS-MC is only a filter for pixels potentially contaminated by the presence of snow. The potential overestimation of snow cover extent should have limited implications for methane emissions, as methane emissions in these regions during the snow season should be a small fraction of global emissions, as discussed above.

6 Perspectives

Several key areas for future improvement of the GIEMS-MC production process were identified. First, taking into account the inter-annual variations of rice paddies would help improve the accuracy and in particular the long-term trend of GIEMS-MC. Ideally, these estimates should be consistent with those used in anthropogenic greenhouse gas emission inventories such as FAOSTAT. Secondly, a better distinction between inundated and dry peatlands would al-

low a more accurate integration of peatlands into GIEMS-MC_{ISW+P}. New satellite data, such as the 2022-launched Surface Water and Ocean Topography (SWOT) with its Ka-band radar interferometer, hold promise for the monitoring of continental surface water area and height at high spatial resolution and temporal sampling (Neeck et al., 2012; Pedinotti et al., 2014; Biancamaria et al., 2016; Prigent et al., 2016; Peral and Esteban-Fernandez, 2018). In particular, either high-resolution SWOT data or water table depth from a hydrological model combined with the 500 m GLWDv2 data could help to better distinguish the inundated from the non-inundated peatlands to improve the integration of non-inundated peatlands in GIEMS-MC_{ISW+P}. In addition, the upcoming NASA-ISRO Synthetic Aperture Radar (NISAR), scheduled for launch in 2025, will provide high-resolution (below 7 m) observations in L-bands and S-bands (Chuang et al., 2016; Adeli et al., 2021). These frequencies are particularly advantageous for mapping of subcanopy inundation in forested wetlands, as they penetrate vegetation more effectively than the Ka-band used for SWOT.

GIEMS-MC dynamics are derived from GIEMS-2, which provides valuable insights into global water surface dynamics with seamless time series of surface water extent. The continuity of GIEMS-2 production holds the potential to extend the temporal coverage of the GIEMS-MC maps. However, no new SSMIS instrument is planned to be launched when the current instruments (F15 to F18) are decommissioned. Adaptations to the GIEMS-2 process, such as the incorporation of Advanced Microwave Scanning Radiometer (AMSR) data, will be required to extend the observation period despite critical changes in satellite overpassing local time and spatial resolution. Other passive microwave future missions are expected to cover all or part of the SSMIS microwave frequency range, such as the MicroWave Imager (MetOp-SG; D'Addio et al., 2014) or the Copernicus Imaging Microwave Radiometer (CIMR; Vanin et al., 2020), offering alternative data sources for GIEMS-MC production but also requiring adjustment to the methodology. In addition, plans to increase the temporal resolution of GIEMS-2 to a 10 d data record could provide a more detailed understanding of wetland dynamics over time.

7 Data availability

The GIEMS-MC dataset in NetCDF format and its documentation are available at <https://doi.org/10.5281/zenodo.13919644> (Bernard et al., 2024a).

8 Conclusion

Despite significant advances in methane measurement and modelling, accurate mapping of wetland extent remains a key challenge. In this context, we introduce GIEMS-

MethaneCentric (GIEMS-MC). It is a new product that improves the temporal variability of the wetland extent by accurately capturing seasonal and interannual dynamics without discontinuities while also enhancing spatial patterns.

GIEMS-2 product was combined with other information to produce GIEMS-MC, a dataset containing spatially and dynamically consistent maps of different methane-emitting aquatic ecosystems. In particular, the GLWDv2 dataset enables the separation of open water surfaces (lakes, rivers, reservoirs) in GIEMS-2, as well as the addition of peatlands not detected by microwave satellite observations used in GIEMS-2 production. Rice paddies are identified using the MIRCA2000 product. Updated coastal zone filtering improves the previous complete masking in the distributed version of GIEMS-2.

GIEMS-MC provides two harmonized times series maps at $0.25^\circ \times 0.25^\circ$ and monthly time steps of wetland surfaces from 1992 to 2020: one representing inundated and saturated wetlands and the other covering all wetlands, including peatlands. In addition, GIEMS-MC provides consistent maps of rice paddies and categories of open permanent water. Information on the dominant vegetation and wetland type for each pixel is also provided, as these factors help improve the understanding and accurate modelling of methane emissions from wetlands.

This comprehensive database will hopefully set a new standard for harmonizing and consistently mapping methane emission from the different aquatic ecosystems.

Supplement. The supplement related to this article is available online at <https://doi.org/10.5194/essd-17-2985-2025-supplement>.

Author contributions. JB, CP, CJ, MS, and EF-C conceived the main ideas of this study. CJ and CP developed and produced the GIEMS-2 data. BL provided the GLWDv2 product. JB, CJ, and CP built the database and performed the numerical analyses. JB drafted the manuscript with input from CP, MS, and EF-C. All authors provided critical feedback and expertise on the manuscript.

Competing interests. The contact author has declared that none of the authors has any competing interests.

Disclaimer. Publisher's note: Copernicus Publications remains neutral with regard to jurisdictional claims made in the text, published maps, institutional affiliations, or any other geographical representation in this paper. While Copernicus Publications makes every effort to include appropriate place names, the final responsibility lies with the authors.

Acknowledgements. The authors would like to thank Pierre Zeiger and Frédéric Frappart for the discussions on their CYGNSS-

derived wetland extent dataset. The authors thank John Melack and the two anonymous referees for their comments and suggestions.

Financial support. Juliette Bernard is funded by a PhD grant from the Institut National des Sciences de l'Univers (INSU) of the Centre National de la Recherche Scientifique (CNRS). Partial funding has been provided by the ESA CCI RECAPP2 project (grant no. 4000123002/18/INB), and a preliminary version of this database has been developed under that contract. The Agence Nationale de la Recherche also provided support through the project Advanced Methane Budget through Multi-constraints and Multi-data streams Modelling (grant no. AMB-M3-ANR-21-CE01-0030). Etienne Fluet-Chouinard was supported by COMPASS-FME, a multi-institutional project supported by the U.S. Department of Energy, Office of Science, Biological and Environmental Research as part of the Environmental System Science Program.

Review statement. This paper was edited by Hanqin Tian and reviewed by John Melack and two anonymous referees.

References

- Adeli, S., Salehi, B., Mahdianpari, M., Quackenbush, L. J., and Chapman, B.: Moving Toward L-Band NASA-ISRO SAR Mission (NISAR) Dense Time Series: Multipolarization Object-Based Classification of Wetlands Using Two Machine Learning Algorithms, *Earth Space Sci.*, 8, e2021EA001742, <https://doi.org/10.1029/2021EA001742>, 2021.
- Aires, F., Miolane, L., Prigent, C., Pham, B., Fluet-Chouinard, E., Lehner, B., and Papa, F.: A Global Dynamic Long-Term Inundation Extent Dataset at High Spatial Resolution Derived through Downscaling of Satellite Observations, *J. Hydrometeorol.*, 18, 1305–1325, <https://doi.org/10.1175/JHM-D-16-0155.1>, 2017.
- Allen, G. H. and Pavelsky, T. M.: Global Extent of Rivers and Streams, *Science*, 361, 585–588, <https://doi.org/10.1126/science.aat0636>, 2018.
- Bao, T., Xu, X., Jia, G., Billesbach, D. P., and Sullivan, R. C.: Much Stronger Tundra Methane Emissions during Autumn Freeze than Spring Thaw, *Global Change Biol.*, 27, 376–387, <https://doi.org/10.1111/gcb.15421>, 2021.
- Bartholomé, E. and Belward, A. S.: GLC2000: A New Approach to Global Land Cover Mapping from Earth Observation Data, *Int. J. Remote Sens.*, 26, 1959–1977, <https://doi.org/10.1080/01431160412331291297>, 2005.
- Bernard, J., Prigent, C., Jimenez, C., Fluet-Chouinard, E., Lehner, B., Salmon, E., Ciais, P., Zhen, Z., Peng, S., and Saunio, M.: GIEMS-MethaneCentric, Zenodo [data set], <https://doi.org/10.5281/zenodo.13919644>, 2024a.
- Bernard, J., Prigent, C., Jimenez, C., Frappart, F., Normandin, C., Zeiger, P., Xi, Y., and Peng, S.: Assessing the Time Variability of GIEMS-2 Satellite-Derived Surface Water Extent over 30 Years, *Front. Remote Sens.*, 5, 1399234, <https://doi.org/10.3389/frsen.2024.1399234>, 2024b.
- Biancamaria, S., Lettenmaier, D. P., and Pavelsky, T. M.: The SWOT Mission and Its Capabilities for Land Hydrology,

- Surv. Geophys., 37, 307–337, <https://doi.org/10.1007/s10712-015-9346-y>, 2016.
- Bousquet, P., Ciais, P., Miller, J. B., Dlugokencky, E. J., Hauglustaine, D. A., Prigent, C., Van Der Werf, G. R., Peylin, P., Brunke, E.-G., Carouge, C., Langenfelds, R. L., Lathière, J., Papa, F., Ramonet, M., Schmidt, M., Steele, L. P., Tyler, S. C., and White, J.: Contribution of Anthropogenic and Natural Sources to Atmospheric Methane Variability, *Nature*, 443, 439–443, <https://doi.org/10.1038/nature05132>, 2006.
- Bridgman, S. D., Cadillo-Quiroz, H., Keller, J. K., and Zhuang, Q.: Methane Emissions from Wetlands: Biogeochemical, Microbial, and Modeling Perspectives from Local to Global Scales, *Global Change Biol.*, 19, 1325–1346, <https://doi.org/10.1111/gcb.12131>, 2013.
- Copernicus Climate Change Service: ERA5 hourly data on single levels from 1950 to present, Copernicus Climate Change Service (C3S) Climate Data Store (CDS), <https://doi.org/10.24381/CDS.68D2BB30>, 2019.
- Canadell, J., Monteiro, P., Costa, M., Cotrim da Cunha, L., Cox, P., Eliseev, A., Henson, S., Ishii, M., Jaccard, S., Koven, C., Lohila, A., Patra, P., Piao, S., Rogelj, J., Syampungani, S., Zaehle, S., and Zickfeld, K.: Global Carbon and other Biogeochemical Cycles and Feedbacks, in: *Climate Change 2021: The Physical Science Basis. Contribution of Working Group I to the Sixth Assessment Report of the Intergovernmental Panel on Climate Change*, edited by: Masson-Delmotte, V., Zhai, P., Pirani, A., Connors, S. L., Péan, C., Berger, S., Caud, N., Chen, Y., Goldfarb, L., Gomis, M. I., Huang, M., Leitzell, K., Lonnoy, E., Matthews, J. B. R., Maycock, T. K., Waterfield, T., Yelekçi, O., Yu, R., and Zhou, B., book Sect. 5, Cambridge University Press, Cambridge, UK and New York, NY, USA, <https://doi.org/10.1017/9781009157896.007>, 2021.
- Carroll, M., Townshend, J., DiMiceli, C., Noojipady, P., and Sohlberg, R.: A New Global Raster Water Mask at 250 m Resolution, *Int. J. Digital Earth*, 2, 291–308, <https://doi.org/10.1080/17538940902951401>, 2009.
- Chapman, B., McDonald, K., Shimada, M., Rosenqvist, A., Schroeder, R., and Hess, L.: Mapping Regional Inundation with Spaceborne L-Band SAR, *Remote Sens.*, 7, 5440–5470, <https://doi.org/10.3390/rs70505440>, 2015.
- Chuang, C.-L., Shaffer, S., Niamsuwan, N., Li, S., Liao, E., Lim, C., Duong, V., Volain, B., Vines, K., Yang, M.-W., and Wheeler, K.: NISAR L-band Digital Electronics Subsystem: A Multichannel System with Distributed Processors for Digital Beam Forming and Mode Dependent Filtering, in: *2016 IEEE Radar Conference (RadarConf)*, 1–5 pp., IEEE, Philadelphia, PA, USA, ISBN 978-1-5090-0863-6, <https://doi.org/10.1109/RADAR.2016.7485225>, 2016.
- D’Addio, S., Kangas, V., Klein, U., Loiselet, M., and Mason, G.: The Microwave Radiometers On-Board MetOp Second Generation Satellites, in: *2014 IEEE Metrology for Aerospace (MetroAeroSpace)*, 599–604 pp., IEEE, Benevento, Italy, ISBN 978-1-4799-2069-3, <https://doi.org/10.1109/MetroAeroSpace.2014.6865995>, 2014.
- Dargie, G. C., Lewis, S. L., Lawson, I. T., Mitchard, E. T. A., Page, S. E., Bocko, Y. E., and Ifo, S. A.: Age, Extent and Carbon Storage of the Central Congo Basin Peatland Complex, *Nature*, 542, 86–90, <https://doi.org/10.1038/nature21048>, 2017.
- Defourny, P., Lamarche, C., Bontemps, S., De Maet, T., Van Bo-gaert, E., Moreau, I., Brockmann, C., Boettcher, M., Kirches, G., Wevers, J., Santoro, M., Ramoino, F., and Arino, O.: Land Cover Climate Change Initiative – Product User Guide v2, Issue 2.0, http://maps.elie.ucl.ac.be/CCI/viewer/download/ESACCI-LC-Ph2-PUGv2_2.0.pdf (last access: 7 June 2025), 2017.
- Di Gregorio, A. and Jansen, L. J.: Land Cover Classification System (LCCS): Classification Concepts and User Manual, <https://www.fao.org/3/x0596e/x0596e00.htm> (last access: 16 September 2024), 2005.
- FAO: FAO Rice Information, Volume 3, FAO, <https://www.fao.org/4/y4347e/y4347e00.htm> (last access: 7 June 2025), 2002.
- Feng, M., Sexton, J. O., Channan, S., and Townshend, J. R.: A Global, High-Resolution (30-m) Inland Water Body Dataset for 2000: First Results of a Topographic–Spectral Classification Algorithm, *Int. J. Digital Earth*, 9, 113–133, <https://doi.org/10.1080/17538947.2015.1026420>, 2016.
- Fennig, K., Schröder, M., Andersson, A., and Hollmann, R.: A Fundamental Climate Data Record of SMMR, SSM/I, and SS-MIS brightness temperatures, *Earth Syst. Sci. Data*, 12, 647–681, <https://doi.org/10.5194/essd-12-647-2020>, 2020.
- Feron, S., Malhotra, A., Bansal, S., Fluet-Chouinard, E., McNicol, G., Knox, S. H., Delwiche, K. B., Cordero, R. R., Ouyang, Z., Zhang, Z., Poulter, B., and Jackson, R. B.: Recent Increases in Annual, Seasonal, and Extreme Methane Fluxes Driven by Changes in Climate and Vegetation in Boreal and Temperate Wetland Ecosystems, *Global Change Biol.*, 30, e17131, <https://doi.org/10.1111/gcb.17131>, 2024.
- Fleischmann, A. S., Papa, F., Fassoni-Andrade, A., Melack, J. M., Wongchuig, S., Paiva, R. C. D., Hamilton, S. K., Fluet-Chouinard, E., Barbedo, R., Aires, F., Al Bitar, A., Bonnet, M.-P., Coe, M., Ferreira-Ferreira, J., Hess, L., Jensen, K., McDonald, K., Ovando, A., Park, E., Parrens, M., Pinel, S., Prigent, C., Resende, A. F., Revel, M., Rosenqvist, A., Rosenqvist, J., Rudorff, C., Silva, T. S. F., Yamazaki, D., and Collischonn, W.: How Much Inundation Occurs in the Amazon River Basin?, *Remote Sens. Environ.*, 278, 113099, <https://doi.org/10.1016/j.rse.2022.113099>, 2022.
- Fluet-Chouinard, E., Lehner, B., Rebelo, L.-M., Papa, F., and Hamilton, S. K.: Development of a Global Inundation Map at High Spatial Resolution from Topographic Downscaling of Coarse-Scale Remote Sensing Data, *Remote Sens. Environ.*, 158, 348–361, <https://doi.org/10.1016/j.rse.2014.10.015>, 2015.
- Foster, J. L., Hall, D. K., Chang, A. T. C., and Rango, A.: An Overview of Passive Microwave Snow Research and Results, *Rev. Geophys.*, 22, 195–208, <https://doi.org/10.1029/RG022i002p00195>, 1984.
- Frappart, F., Biancamaria, S., Normandin, C., Blarel, F., Bourrel, L., Aumont, M., Azemar, P., Vu, P.-L., Le Toan, T., Lubac, B., and Darrozes, J.: Influence of Recent Climatic Events on the Surface Water Storage of the Tonle Sap Lake, *Sci. Total Environ.*, 636, 1520–1533, <https://doi.org/10.1016/j.scitotenv.2018.04.326>, 2018.
- Friedl, M., McIver, D., Hodges, J., Zhang, X., Muchoney, D., Strahler, A., Woodcock, C., Gopal, S., Schneider, A., Cooper, A., Baccini, A., Gao, F., and Schaaf, C.: Global Land Cover Mapping from MODIS: Algorithms and Early Results, *Remote*

- Sens. Environ., 83, 287–302, [https://doi.org/10.1016/S0034-4257\(02\)00078-0](https://doi.org/10.1016/S0034-4257(02)00078-0), 2002.
- Ge, M., Korrensalo, A., Laiho, R., Kohl, L., Lohila, A., Pihlatie, M., Li, X., Laine, A. M., Anttila, J., Putkinen, A., Wang, W., and Koskinen, M.: Plant-Mediated CH₄ Exchange in Wetlands: A Review of Mechanisms and Measurement Methods with Implications for Modelling, *Sci. Total Environ.*, 914, 169662, <https://doi.org/10.1016/j.scitotenv.2023.169662>, 2024.
- Gerlein-Safdi, C. and Ruf, C.: CYGNSS-based inundation maps of the Pantanal and the Sudd wetlands from June 2017 to December 2019, Zenodo, <https://doi.org/10.5281/ZENODO.5621107>, 2021.
- Gerlein-Safdi, C., Bloom, A. A., Plant, G., Kort, E. A., and Ruf, C. S.: Improving Representation of Tropical Wetland Methane Emissions With CYGNSS Inundation Maps, *Global Biogeochem. Cy.*, 35, 12, <https://doi.org/10.1029/2020GB006890>, 2021.
- Girkin, N. T., Siegenthaler, A., Lopez, O., Stott, A., Ostle, N., Gauci, V., and Sjögersten, S.: Plant Root Carbon Inputs Drive Methane Production in Tropical Peatlands, *Sci. Rep.*, 15, 3244, <https://doi.org/10.1038/s41598-025-87467-w>, 2025.
- Gumbrecht, T., Roman-Cuesta, R. M., Verchot, L., Herold, M., Wittmann, F., Householder, E., Herold, N., and Muriyars, D.: An Expert System Model for Mapping Tropical Wetlands and Peatlands Reveals South America as the Largest Contributor, *Global Change Biol.*, 23, 3581–3599, <https://doi.org/10.1111/gcb.13689>, 2017.
- Harper, K. L., Lamarche, C., Hartley, A., Peylin, P., Otlé, C., Bastrikov, V., San Martín, R., Bohnenstengel, S. I., Kirches, G., Boettcher, M., Shevchuk, R., Brockmann, C., and Defourny, P.: A 29-year time series of annual 300 m resolution plant-functional-type maps for climate models, *Earth Syst. Sci. Data*, 15, 1465–1499, <https://doi.org/10.5194/essd-15-1465-2023>, 2023.
- Hastie, A., Householder, J. E., Honorio Coronado, E. N., Hidalgo Pizango, C. G., Herrera, R., Lähteenoja, O., De Jong, J., Winton, R. S., Aymard Corredor, G. A., Reyna, J., Montoya, E., Pauku, S., Mitchard, E. T. A., Åkesson, C. M., Baker, T. R., Cole, L. E. S., Córdova Oroche, C. J., Dávila, N., Águila, J. D., Draper, F. C., Fluet-Chouinard, E., Grández, J., Janovec, J. P., Reyna, D., W Tobler, M., Del Castillo Torres, D., Roucoux, K. H., Wheeler, C. E., Fernandez Piedade, M. T., Schöngart, J., Wittmann, F., Van Der Zon, M., and Lawson, I. T.: A New Data-Driven Map Predicts Substantial Undocumented Peatland Areas in Amazonia, *Environ. Res. Lett.*, 19, 094019, <https://doi.org/10.1088/1748-9326/ad677b>, 2024.
- Hengl, T., Mendes de Jesus, J., Heuvelink, G. B. M., Ruiperez Gonzalez, M., Kilibarda, M., Blagotić, A., Shangquan, W., Wright, M. N., Geng, X., Bauer-Marschallinger, B., Guevara, M. A., Vargas, R., MacMillan, R. A., Batjes, N. H., Leenaars, J. G. B., Ribeiro, E., Wheeler, I., Mantel, S., and Kempen, B.: SoilGrids250m: Global Gridded Soil Information Based on Machine Learning, *PLOS ONE*, 12, e0169748, <https://doi.org/10.1371/journal.pone.0169748>, 2017.
- Hersbach, H., Bell, B., Berrisford, P., Hirahara, S., Horányi, A., Muñoz-Sabater, J., Nicolas, J., Peubey, C., Radu, R., Schepers, D., Simmons, A., Soci, C., Abdalla, S., Abellan, X., Balsamo, G., Bechtold, P., Biavati, G., Bidlot, J., Bonavita, M., De Chiara, G., Dahlgren, P., Dee, D., Diamantakis, M., Dragani, R., Flemming, J., Forbes, R., Fuentes, M., Geer, A., Haimberger, L., Healy, S., Hogan, R. J., Hólm, E., Janisková, M., Keeley, S., Laloyaux, P., Lopez, P., Lupu, C., Radnoti, G., De Rosnay, P., Rozum, I., Vamborg, F., Villaume, S., and Thépaut, J.-N.: The ERA5 Global Reanalysis, *Q. J. Roy. Meteorol. Soc.*, 146, 1999–2049, <https://doi.org/10.1002/qj.3803>, 2020.
- Hu, S., Niu, Z., and Chen, Y.: Global Wetland Datasets: A Review, *Wetlands*, 37, 807–817, <https://doi.org/10.1007/s13157-017-0927-z>, 2017.
- Hugelius, G., Tarnocai, C., Broll, G., Canadell, J. G., Kuhry, P., and Swanson, D. K.: The Northern Circumpolar Soil Carbon Database: spatially distributed datasets of soil coverage and soil carbon storage in the northern permafrost regions, *Earth Syst. Sci. Data*, 5, 3–13, <https://doi.org/10.5194/essd-5-3-2013>, 2013.
- Ito, A., Li, T., Qin, Z., Melton, J. R., Tian, H., Kleinen, T., Zhang, W., Zhang, Z., Joos, F., Ciais, P., Hopcroft, P. O., Beerling, D. J., Liu, X., Zhuang, Q., Zhu, Q., Peng, C., Chang, K.-Y., Fluet-Chouinard, E., McNicol, G., Patra, P., Poulter, B., Sitch, S., Riley, W., and Zhu, Q.: Cold-Season Methane Fluxes Simulated by GCP-CH₄ Models, *Geophys. Res. Lett.*, 50, e2023GL103037, <https://doi.org/10.1029/2023GL103037>, 2023.
- Janssens-Maenhout, G., Crippa, M., Guizzardi, D., Muntean, M., Schaaf, E., Dentener, F., Bergamaschi, P., Pagliari, V., Olivier, J. G. J., Peters, J. A. H. W., van Aardenne, J. A., Monni, S., Doering, U., Petrescu, A. M. R., Solazzo, E., and Oreggioni, G. D.: EDGAR v4.3.2 Global Atlas of the three major greenhouse gas emissions for the period 1970–2012, *Earth Syst. Sci. Data*, 11, 959–1002, <https://doi.org/10.5194/essd-11-959-2019>, 2019.
- Jensen, K. and McDonald, K.: Surface Water Microwave Product Series Version 3: A Near-Real Time and 25-Year Historical Global Inundated Area Fraction Time Series From Active and Passive Microwave Remote Sensing, *IEEE Geosci. Remote Sens. Lett.*, 16, 1402–1406, <https://doi.org/10.1109/LGRS.2019.2898779>, 2019.
- Kouki, K., Luojus, K., and Riihelä, A.: Evaluation of snow cover properties in ERA5 and ERA5-Land with several satellite-based datasets in the Northern Hemisphere in spring 1982–2018, *The Cryosphere*, 17, 5007–5026, <https://doi.org/10.5194/tc-17-5007-2023>, 2023.
- Laborte, A. G., Gutierrez, M. A., Balanza, J. G., Saito, K., Zwart, S. J., Boschetti, M., Murty, M., Villano, L., Aunario, J. K., Reinke, R., Koo, J., Hijmans, R. J., and Nelson, A.: RiceAtlas, a Spatial Database of Global Rice Calendars and Production, *Sci. Data*, 4, 170074, <https://doi.org/10.1038/sdata.2017.74>, 2017.
- Lan, X., K.W., T., and E.J., D.: Trends in globally-averaged CH₄, N₂O, and SF₆ determined from NOAA Global Monitoring Laboratory measurements, *NOAA GML*, <https://doi.org/10.15138/P8XG-AA10>, 2024.
- Lehner, B. and Döll, P.: Development and Validation of a Global Database of Lakes, Reservoirs and Wetlands, *J. Hydrol.*, 296, 1–22, <https://doi.org/10.1016/j.jhydrol.2004.03.028>, 2004.
- Lehner, B., Beames, P., Mulligan, M., Zarfl, C., De Felice, L., Van Soesbergen, A., Thieme, M., Garcia De Leaniz, C., Anand, M., Belletti, B., Brauman, K. A., Januchowski-Hartley, S. R., Lyon, K., Mandle, L., Mazany-Wright, N., Messenger, M. L., Pavelsky, T., Pekel, J.-F., Wang, J., Wen, Q., Wishart, M., Xing, T., Yang, X., and Higgins, J.: The Global Dam Watch Database of River Barrier and Reservoir Information for Large-Scale Applications, *Sci. Data*, 11, 1069, <https://doi.org/10.1038/s41597-024-03752-9>, 2024.

- Lehner, B., Anand, M., Fluet-Chouinard, E., Tan, F., Aires, F., Allen, G. H., Bousquet, P., Canadell, J. G., Davidson, N., Ding, M., Finlayson, C. M., Gumbrecht, T., Hilarides, L., Hugelius, G., Jackson, R. B., Korver, M. C., Liu, L., McIntyre, P. B., Nagy, S., Olefeldt, D., Pavelsky, T. M., Pekel, J.-F., Poulter, B., Prigent, C., Wang, J., Worthington, T. A., Yamazaki, D., Zhang, X., and Thieme, M.: Mapping the world's inland surface waters: an upgrade to the Global Lakes and Wetlands Database (GLWD v2), *Earth Syst. Sci. Data*, 17, 2277–2329, <https://doi.org/10.5194/essd-17-2277-2025>, 2025a.
- Lehner, B., Anand, M., Fluet-Chouinard, E., Tan, F., Aires, F., Allen, G. H., Bousquet, P., Canadell, J. G., Davidson, N., Ding, M., Finlayson, C. M., Gumbrecht, T., Hilarides, L., Hugelius, G., Jackson, R. B., Korver, M. C., Liu, L., McIntyre, P. B., Nagy, S., Olefeldt, D., Pavelsky, T. M., Pekel, J.-F., Poulter, B., Prigent, C., Wang, J., Worthington, T. A., Yamazaki, D., Zhang, X., and Thieme, M.: Global Lakes and Wetlands Database (GLWD) version 2.0, figshare, <https://doi.org/10.6084/M9.FIGSHARE.28519994.V1>, 2025b.
- Linke, S., Lehner, B., Ouellet Dallaire, C., Ariwi, J., Grill, G., Anand, M., Beames, P., Burchard-Levine, V., Maxwell, S., Moidu, H., Tan, F., and Thieme, M.: Global Hydro-Environmental Sub-Basin and River Reach Characteristics at High Spatial Resolution, *Sci. Data*, 6, 283, <https://doi.org/10.1038/s41597-019-0300-6>, 2019.
- Lourenco, M., Fitchett, J. M., and Woodborne, S.: Peat Definitions: A Critical Review, *Prog. Phys. Geogr.-Earth Environ.*, 47, 506–520, <https://doi.org/10.1177/03091333221118353>, 2023.
- Loveland, T. R., Reed, B. C., Brown, J. F., Ohlen, D. O., Zhu, Z., Yang, L., and Merchant, J. W.: Development of a Global Land Cover Characteristics Database and IGBP DISCover from 1 Km AVHRR Data, *Int. J. Remote Sens.*, 21, 1303–1330, <https://doi.org/10.1080/014311600210191>, 2000.
- Maclean, J., Hardy, B., and Hettel, G.: GRISP (Global Rice Science Partnership). 2013. Rice almanac, 4th Edn., Los Baños (Philippines): International Rice Research Institute, 283 p., http://books.irri.org/9789712203008_content.pdf (last access: 6 May 2024), 2013.
- McNicol, G., Fluet-Chouinard, E., Ouyang, Z., Knox, S., Zhang, Z., Aalto, T., Bansal, S., Chang, K.-Y., Chen, M., Delwiche, K., Feron, S., Goeckede, M., Liu, J., Malhotra, A., Melton, J. R., Riley, W., Vargas, R., Yuan, K., Ying, Q., Zhu, Q., Alekseychik, P., Aurela, M., Billesbach, D. P., Campbell, D. I., Chen, J., Chu, H., Desai, A. R., Euskirchen, E., Goodrich, J., Griffis, T., Helbig, M., Hirano, T., Iwata, H., Jurasinski, G., King, J., Koebisch, F., Kolka, R., Krauss, K., Lohila, A., Mammarella, I., Nilson, M., Noormets, A., Oechel, W., Peichl, M., Sachs, T., Sakabe, A., Schulze, C., Sonnentag, O., Sullivan, R. C., Tuittila, E.-S., Ueyama, M., Vesala, T., Ward, E., Wille, C., Wong, G. X., Zona, D., Windham-Myers, L., Poulter, B., and Jackson, R. B.: Upscaling Wetland Methane Emissions From the FLUXNET-CH4 Eddy Covariance Network (UpCH4 v1.0): Model Development, Network Assessment, and Budget Comparison, *AGU Adv.*, 4, e2023AV000956, <https://doi.org/10.1029/2023AV000956>, 2023.
- Melton, J. R., Wania, R., Hodson, E. L., Poulter, B., Ringeval, B., Spahni, R., Bohn, T., Avis, C. A., Beerling, D. J., Chen, G., Eliseev, A. V., Denisov, S. N., Hopcroft, P. O., Lettenmaier, D. P., Riley, W. J., Singarayer, J. S., Subin, Z. M., Tian, H., Zürcher, S., Brovkin, V., van Bodegom, P. M., Kleinen, T., Yu, Z. C., and Kaplan, J. O.: Present state of global wetland extent and wetland methane modelling: conclusions from a model inter-comparison project (WETCHIMP), *Biogeosciences*, 10, 753–788, <https://doi.org/10.5194/bg-10-753-2013>, 2013.
- Messenger, M. L., Lehner, B., Grill, G., Nedeva, I., and Schmitt, O.: Estimating the Volume and Age of Water Stored in Global Lakes Using a Geo-Statistical Approach, *Nat. Commun.*, 7, 13603, <https://doi.org/10.1038/ncomms13603>, 2016.
- Neeck, S. P., Lindstrom, E. J., Vaze, P. V., and Fu, L.-L.: Surface Water and Ocean Topography (SWOT) Mission, in: *SPIE Remote Sensing*, edited by: Meynart, R., Neeck, S. P., and Shimoda, H., p. 85330G, Edinburgh, United Kingdom, <https://doi.org/10.1117/12.981151>, 2012.
- Nisbet, E. G., Dlugokencky, E. J., Manning, M. R., Lowry, D., Fisher, R. E., France, J. L., Michel, S. E., Miller, J. B., White, J. W. C., Vaughn, B., Bousquet, P., Pyle, J. A., Warwick, N. J., Cain, M., Brownlow, R., Zazzeri, G., Lanoisellé, M., Manning, A. C., Gloor, E., Worthy, D. E. J., Brunke, E.-G., Labuschagne, C., Wolff, E. W., and Ganesan, A. L.: Rising Atmospheric Methane: 2007–2014 Growth and Isotopic Shift, *Global Biogeochem. Cy.*, 30, 1356–1370, <https://doi.org/10.1002/2016GB005406>, 2016.
- Nisbet, E. G., Manning, M. R., Dlugokencky, E. J., Fisher, R. E., Lowry, D., Michel, S. E., Myhre, C. L., Platt, S. M., Allen, G., Bousquet, P., Brownlow, R., Cain, M., France, J. L., Hermansen, O., Hossaini, R., Jones, A. E., Levin, I., Manning, A. C., Myhre, G., Pyle, J. A., Vaughn, B. H., Warwick, N. J., and White, J. W. C.: Very Strong Atmospheric Methane Growth in the 4 Years 2014–2017: Implications for the Paris Agreement, *Global Biogeochem. Cy.*, 33, 318–342, <https://doi.org/10.1029/2018GB006009>, 2019.
- Normandin, C., Frappart, F., Lubac, B., Bélanger, S., Marieu, V., Blarel, F., Robinet, A., and Guiastron-Faugas, L.: Quantification of surface water volume changes in the Mackenzie Delta using satellite multi-mission data, *Hydrol. Earth Syst. Sci.*, 22, 1543–1561, <https://doi.org/10.5194/hess-22-1543-2018>, 2018.
- Normandin, C., Frappart, F., Bourrel, L., Diepkilé, A. T., Mougin, E., Zwarts, L., Blarel, F., Egon, F., and Wigneron, J.-P.: Quantification of Surface Water Extent and Volume in the Inner Niger Delta (IND) over 2000–2022 Using Multispectral Imagery and Radar Altimetry, *Geocart. Int.*, 39, 2311203, <https://doi.org/10.1080/10106049.2024.2311203>, 2024.
- Obled, C. and Zin, I.: TOPMODEL : principes de fonctionnement et application, *La Houille Blanche*, 90, 65–77, <https://doi.org/10.1051/lhb:200401009>, 2004.
- Olefeldt, D., Hovemyr, M., Kuhn, M., Bastviken, D., Bohn, T., Connolly, J., Crill, P., Euskirchen, E., Finkelstein, S., Genet, H., Grosse, G., Harris, L., Heffernan, L., Helbig, M., Hugelius, G., Hutchins, R., Juutinen, S., Lara, M., Malhotra, A., Manies, K., McGuire, D., Natali, S., O'Donnell, J., Parmentier, F.-J., Räsänen, A., Schädel, C., Sonnentag, O., Strack, M., Tank, S., Treat, C., Varner, R., Virtanen, T., Warren, R., and Watts, J.:

- The fractional land cover estimates from the Boreal-Arctic Wetland and Lake Dataset (BAWLD), 2021, NSF Arctic Data Center, <https://doi.org/10.18739/A2C824F9X>, 2021a.
- Olefeldt, D., Hovemyr, M., Kuhn, M. A., Bastviken, D., Bohn, T. J., Connolly, J., Crill, P., Euskirchen, E. S., Finkelstein, S. A., Genet, H., Grosse, G., Harris, L. I., Heffernan, L., Helbig, M., Hugelius, G., Hutchins, R., Juutinen, S., Lara, M. J., Malhotra, A., Manies, K., McGuire, A. D., Natali, S. M., O'Donnell, J. A., Parmentier, F.-J. W., Räsänen, A., Schädel, C., Sonnentag, O., Strack, M., Tank, S. E., Treat, C., Varner, R. K., Virtanen, T., Warren, R. K., and Watts, J. D.: The Boreal–Arctic Wetland and Lake Dataset (BAWLD), *Earth Syst. Sci. Data*, 13, 5127–5149, <https://doi.org/10.5194/essd-13-5127-2021>, 2021b.
- Pangala, S. R., Enrich-Prast, A., Basso, L. S., Peixoto, R. B., Bastviken, D., Hornibrook, E. R. C., Gatti, L. V., Marotta, H., Calazans, L. S. B., Sakuragui, C. M., Bastos, W. R., Malm, O., Gloor, E., Miller, J. B., and Gauci, V.: Large Emissions from Floodplain Trees Close the Amazon Methane Budget, *Nature*, 552, 230–234, <https://doi.org/10.1038/nature24639>, 2017.
- Papa, F., Prigent, C., Durand, F., and Rossow, W. B.: Wetland Dynamics Using a Suite of Satellite Observations: A Case Study of Application and Evaluation for the Indian Subcontinent, *Geophys. Res. Lett.*, 33, 2006GL025767, <https://doi.org/10.1029/2006GL025767>, 2006.
- Papa, F., Güntner, A., Frappart, F., Prigent, C., and Rossow, W. B.: Variations of Surface Water Extent and Water Storage in Large River Basins: A Comparison of Different Global Data Sources, *Geophys. Res. Lett.*, 35, 2008GL033857, <https://doi.org/10.1029/2008GL033857>, 2008.
- Papa, F., Prigent, C., Aires, F., Jimenez, C., Rossow, W. B., and Matthews, E.: Interannual Variability of Surface Water Extent at the Global Scale, 1993–2004, *J. Geophys. Res.-Atmos.*, 115, 2009JD012674, <https://doi.org/10.1029/2009JD012674>, 2010.
- Pedinotti, V., Boone, A., Ricci, S., Biancamaria, S., and Mognard, N.: Assimilation of satellite data to optimize large-scale hydrological model parameters: a case study for the SWOT mission, *Hydrol. Earth Syst. Sci.*, 18, 4485–4507, <https://doi.org/10.5194/hess-18-4485-2014>, 2014.
- Pekel, J.-F., Cottam, A., Gorelick, N., and Belward, A. S.: High-Resolution Mapping of Global Surface Water and Its Long-Term Changes, *Nature*, 540, 418–422, <https://doi.org/10.1038/nature20584>, 2016.
- Peltola, O., Vesala, T., Gao, Y., Rätty, O., Alekseychik, P., Aurela, M., Chojnicki, B., Desai, A. R., Dolman, A. J., Euskirchen, E. S., Friborg, T., Göckede, M., Helbig, M., Humphreys, E., Jackson, R. B., Jocher, G., Joos, F., Klatt, J., Knox, S. H., Kowalska, N., Kutzbach, L., Lienert, S., Lohila, A., Mammarella, I., Nadeau, D. F., Nilsson, M. B., Oechel, W. C., Peichl, M., Pypker, T., Quinton, W., Rinne, J., Sachs, T., Samson, M., Schmid, H. P., Sonnentag, O., Wille, C., Zona, D., and Aalto, T.: Monthly gridded data product of northern wetland methane emissions based on up-scaling eddy covariance observations, *Earth Syst. Sci. Data*, 11, 1263–1289, <https://doi.org/10.5194/essd-11-1263-2019>, 2019.
- Peral, E. and Esteban-Fernandez, D.: Swot Mission Performance and Error Budget, in: *IGARSS 2018–2018 IEEE International Geoscience and Remote Sensing Symposium*, 8625–8628 pp., IEEE, Valencia, ISBN 978-1-5386-7150-4, <https://doi.org/10.1109/IGARSS.2018.8517385>, 2018.
- Pham-Duc, B., Prigent, C., Aires, F., and Papa, F.: Comparisons of Global Terrestrial Surface Water Datasets over 15 Years, *J. Hydrometeorol.*, 18, 993–1007, <https://doi.org/10.1175/JHM-D-16-0206.1>, 2017.
- Portmann, F. T., Siebert, S., and Döll, P.: MIRCA2000, Zenodo, <https://doi.org/10.5281/ZENODO.7422506>, 2010a.
- Portmann, F. T., Siebert, S., and Döll, P.: MIRCA2000-Global Monthly Irrigated and Rainfed Crop Areas around the Year 2000: A New High-Resolution Data Set for Agricultural and Hydrological Modeling: MONTHLY IRRIGATED AND RAINFED CROP AREAS, *Global Biogeochem. Cy.*, 24, 1, <https://doi.org/10.1029/2008GB003435>, 2010b.
- Poulter, B., Bousquet, P., Canadell, J. G., Ciais, P., Peregon, A., Saunio, M., Arora, V. K., Beerling, D. J., Brovkin, V., Jones, C. D., Joos, F., Gedney, N., Ito, A., Kleinen, T., Koven, C. D., McDonald, K., Melton, J. R., Peng, C., Peng, S., Prigent, C., Schroeder, R., Riley, W. J., Saito, M., Spahni, R., Tian, H., Taylor, L., Viovy, N., Wilton, D., Wiltshire, A., Xu, X., Zhang, B., Zhang, Z., and Zhu, Q.: Global Wetland Contribution to 2000–2012 Atmospheric Methane Growth Rate Dynamics, *Environ. Res. Lett.*, 12, 094013, <https://doi.org/10.1088/1748-9326/aa8391>, 2017.
- Prigent, C., Matthews, E., Aires, F., and Rossow, W. B.: Remote Sensing of Global Wetland Dynamics with Multiple Satellite Data Sets, *Geophys. Res. Lett.*, 28, 4631–4634, <https://doi.org/10.1029/2001GL013263>, 2001.
- Prigent, C., Papa, F., Aires, F., Rossow, W. B., and Matthews, E.: Global Inundation Dynamics Inferred from Multiple Satellite Observations, 1993–2000, *J. Geophys. Res.*, 112, D12107, <https://doi.org/10.1029/2006JD007847>, 2007.
- Prigent, C., Lettenmaier, D. P., Aires, F., and Papa, F.: Toward a High-Resolution Monitoring of Continental Surface Water Extent and Dynamics, at Global Scale: From GIEMS (Global Inundation Extent from Multi-Satellites) to SWOT (Surface Water Ocean Topography), *Surv. Geophys.*, 37, 339–355, <https://doi.org/10.1007/s10712-015-9339-x>, 2016.
- Prigent, C., Jimenez, C., and Bousquet, P.: Satellite-Derived Global Surface Water Extent and Dynamics Over the Last 25 Years (GIEMS-2), *J. Geophys. Res.-Atmos.*, 125, e2019JD030711, <https://doi.org/10.1029/2019JD030711>, 2020.
- Ringeval, B., Decharme, B., Piao, S. L., Ciais, P., Papa, F., de Noblet-Ducoudré, N., Prigent, C., Friedlingstein, P., Gouttevin, I., Koven, C., and Ducharme, A.: Modelling sub-grid wetland in the ORCHIDEE global land surface model: evaluation against river discharges and remotely sensed data, *Geosci. Model Dev.*, 5, 941–962, <https://doi.org/10.5194/gmd-5-941-2012>, 2012.
- Rosenqvist, J., Rosenqvist, A., Jensen, K., and McDonald, K.: Mapping of Maximum and Minimum Inundation Extents in the Amazon Basin 2014–2017 with ALOS-2 PALSAR-2 ScanSAR Time-Series Data, *Remote Sens.*, 12, 1326, <https://doi.org/10.3390/rs12081326>, 2020.
- Rößger, N., Sachs, T., Wille, C., Boike, J., and Kutzbach, L.: Seasonal Increase of Methane Emissions Linked to Warming in Siberian Tundra, *Nat. Clim. Change*, 12, 1031–1036, <https://doi.org/10.1038/s41558-022-01512-4>, 2022.
- Salmon, J., Friedl, M. A., Frohking, S., Wisser, D., and Douglas, E. M.: Global Rain-Fed, Irrigated, and Paddy Croplands: A New High Resolution Map Derived from Remote Sensing, *Crop In-*

- ventories and Climate Data, *Int. J. Appl. Earth Observ. Geoinfo.*, 38, 321–334, <https://doi.org/10.1016/j.jag.2015.01.014>, 2015.
- Saunois, M., Stavert, A. R., Poulter, B., Bousquet, P., Canadell, J. G., Jackson, R. B., Raymond, P. A., Dlugokencky, E. J., Houwel-ling, S., Patra, P. K., Ciais, P., Arora, V. K., Bastviken, D., Bergamaschi, P., Blake, D. R., Brailsford, G., Bruhwiler, L., Carlson, K. M., Carrol, M., Castaldi, S., Chandra, N., Crevoisier, C., Crill, P. M., Covey, K., Curry, C. L., Etiope, G., Frankenberg, C., Gedney, N., Hegglin, M. I., Höglund-Isaksson, L., Hugelius, G., Ishizawa, M., Ito, A., Janssens-Maenhout, G., Jensen, K. M., Joos, F., Kleinen, T., Krummel, P. B., Langenfelds, R. L., Laruelle, G. G., Liu, L., Machida, T., Maksyutov, S., McDona-ld, K. C., McNorton, J., Miller, P. A., Melton, J. R., Morino, I., Müller, J., Murguía-Flores, F., Naik, V., Niwa, Y., Noce, S., O'Doherty, S., Parker, R. J., Peng, C., Peng, S., Peters, G. P., Prigent, C., Prinn, R., Ramonet, M., Regnier, P., Riley, W. J., Rosentreter, J. A., Segers, A., Simpson, I. J., Shi, H., Smith, S. J., Steele, L. P., Thornton, B. F., Tian, H., Tohjima, Y., Tubiello, F. N., Tsuruta, A., Viovy, N., Voulgarakis, A., Weber, T. S., van Weele, M., van der Werf, G. R., Weiss, R. F., Worthy, D., Wunch, D., Yin, Y., Yoshida, Y., Zhang, W., Zhang, Z., Zhao, Y., Zheng, B., Zhu, Q., Zhu, Q., and Zhuang, Q.: The Global Methane Budget 2000–2017, *Earth Syst. Sci. Data*, 12, 1561–1623, <https://doi.org/10.5194/essd-12-1561-2020>, 2020.
- Saunois, M., Martinez, A., Poulter, B., Zhang, Z., Raymond, P. A., Regnier, P., Canadell, J. G., Jackson, R. B., Patra, P. K., Bous-quet, P., Ciais, P., Dlugokencky, E. J., Lan, X., Allen, G. H., Bastviken, D., Beerling, D. J., Belikov, D. A., Blake, D. R., Castaldi, S., Crippa, M., Deemer, B. R., Dennison, F., Etiope, G., Gedney, N., Höglund-Isaksson, L., Holgersson, M. A., Hopcroft, P. O., Hugelius, G., Ito, A., Jain, A. K., Janardanan, R., John-son, M. S., Kleinen, T., Krummel, P. B., Lauerwald, R., Li, T., Liu, X., McDonald, K. C., Melton, J. R., Mühle, J., Müller, J., Murguía-Flores, F., Niwa, Y., Noce, S., Pan, S., Parker, R. J., Peng, C., Ramonet, M., Riley, W. J., Rocher-Ros, G., Rosen- treter, J. A., Sasakawa, M., Segers, A., Smith, S. J., Stanley, E. H., Thanwerdas, J., Tian, H., Tsuruta, A., Tubiello, F. N., Weber, T. S., van der Werf, G. R., Worthy, D. E. J., Xi, Y., Yoshida, Y., Zhang, W., Zheng, B., Zhu, Q., Zhu, Q., and Zhuang, Q.: Global Methane Budget 2000–2020, *Earth Syst. Sci. Data*, 17, 1873–1958, <https://doi.org/10.5194/essd-17-1873-2025>, 2025.
- Schroeder, R., McDonald, K., Chapman, B., Jensen, K., Podest, E., Tessler, Z., Bohn, T., and Zimmermann, R.: Devel- opment and Evaluation of a Multi-Year Fractional Sur- face Water Data Set Derived from Active/Passive Mi- crowave Remote Sensing Data, *Remote Sens.*, 7, 16688–16732, <https://doi.org/10.3390/rs71215843>, 2015.
- Szopa, S., Naik, V., Adhikary, B., Artaxo, P., Bernsten, T., Collins, W., Fuzzi, S., Gallardo, L., Kiendler-Scharr, A., Klimont, Z., Liao, H., Unger, N., and Zanis, P.: Short-Lived Climate Forcers, in: *Climate Change 2021: The Physical Science Bas- is. Contribution of Working Group I to the Sixth Assess- ment Report of the Intergovernmental Panel on Climate Change*, edited by: Masson-Delmotte, V., Zhai, P., Pirani, A., Con- nors, S. L., Péan, C., Berger, S., Caud, N., Chen, Y., Gold- farb, L., Gomis, M. I., Huang, M., Leitzell, K., Lonnoy, E., Matthews, J. B. R., Maycock, T. K., Waterfield, T., Yelekçi, O., Yu, R., and Zhou, B., book Sect. 6, Cambridge Uni- versity Press, Cambridge, UK and New York, NY, USA, <https://doi.org/10.1017/9781009157896.008>, 2021.
- Thornton, B. F., Wik, M., and Crill, P. M.: Double-counting Challenges the Accuracy of High-latitude Methane Inventories, *Geophys. Res. Lett.*, 43, 12569–12577, <https://doi.org/10.1002/2016GL071772>, 2016.
- Tootchi, A., Jost, A., and Ducharme, A.: Multi-source global wetland maps combining surface water imagery and ground- water constraints, *Earth Syst. Sci. Data*, 11, 189–220, <https://doi.org/10.5194/essd-11-189-2019>, 2019.
- Tuanmu, M.-N. and Jetz, W.: A Global 1-km Consensus Land-cover Product for Biodiversity and Ecosystem Modelling, *Global Ecol. Biogeogr.*, 23, 1031–1045, <https://doi.org/10.1111/geb.12182>, 2014.
- Vanin, F., Laberinti, P., Donlon, C., Fiorelli, B., Barat, I., Sole, M. P., Palladino, M., Eggers, P., Rudolph, T., and Galeazzi, C.: Coper- nicus Imaging Microwave Radiometer (CIMR): System Aspects and Technological Challenges, in: *IGARSS 2020–2020 IEEE In- ternational Geoscience and Remote Sensing Symposium*, 6535–6538 pp., IEEE, Waikoloa, HI, USA, ISBN 978-1-72816-374-1, <https://doi.org/10.1109/IGARSS39084.2020.9324259>, 2020.
- Vroom, R., Van Den Berg, M., Pangala, S., Van Der Scheer, O., and Sorrell, B.: Physiological Processes Affecting Methane Transport by Wetland Vegetation – A Review, *Aqua. Bot.*, 182, 103547, <https://doi.org/10.1016/j.aquabot.2022.103547>, 2022.
- Wania, R., Melton, J. R., Hodson, E. L., Poulter, B., Ringeval, B., Spahni, R., Bohn, T., Avis, C. A., Chen, G., Eliseev, A. V., Hopcroft, P. O., Riley, W. J., Subin, Z. M., Tian, H., van Bode- gom, P. M., Kleinen, T., Yu, Z. C., Singarayer, J. S., Zürcher, S., Lettenmaier, D. P., Beerling, D. J., Denisov, S. N., Prigent, C., Papa, F., and Kaplan, J. O.: Present state of global wetland ex- tent and wetland methane modelling: methodology of a model inter-comparison project (WETCHIMP), *Geosci. Model Dev.*, 6, 617–641, <https://doi.org/10.5194/gmd-6-617-2013>, 2013.
- Widhalm, B., Bartsch, A., and Heim, B.: A Novel Approach for the Characterization of Tundra Wetland Regions with C- band SAR Satellite Data, *Int. J. Remote Sens.*, 36, 5537–5556, <https://doi.org/10.1080/01431161.2015.1101505>, 2015.
- Xi, Y., Peng, S., Ducharme, A., Ciais, P., Gumbrecht, T., Jimenez, C., Poulter, B., Prigent, C., Qiu, C., Saunois, M., and Zhang, Z.: Gridded Maps of Wetlands Dynamics over Mid-Low Lat- itudes for 1980–2020 Based on TOPMODEL, *Sci. Data*, 9, 347, <https://doi.org/10.1038/s41597-022-01460-w>, 2022.
- Xu, J., Morris, P. J., Liu, J., and Holden, J.: PEATMAP: Refining Estimates of Global Peatland Distribution Based on a Meta-Analysis, *CATENA*, 160, 134–140, <https://doi.org/10.1016/j.catena.2017.09.010>, 2018.
- Zeiger, P.: Clustering and inundation maps based on CYGNSS re- flectivity, *Odatis*, <https://doi.org/10.6096/3003>, 2023.
- Zeiger, P., Frappart, F., Darrozes, J., Prigent, C., Jiménez, C., and Bourrel, L.: Weekly Mapping of Surface Wa- ter Extent in the Intertropical Wetlands Using Space- borne GNSS Reflectometry, *J. Hydrol.*, 626, 130305, <https://doi.org/10.1016/j.jhydrol.2023.130305>, 2023.
- Zhang, B., Tian, H., Lu, C., Chen, G., Pan, S., Anderson, C., and Poulter, B.: Methane Emissions from Global Wetlands: An Assessment of the Uncertainty Associated with Various Wetland Extent Data Sets, *Atmos. Environ.*, 165, 310–321, <https://doi.org/10.1016/j.atmosenv.2017.07.001>, 2017.

- Zhang, Z., Fluet-Chouinard, E., Jensen, K., McDonald, K., Hugelius, G., Gumbricht, T., Carroll, M., Prigent, C., Bartsch, A., and Poulter, B.: Development of a global dataset of Wetland Area and Dynamics for Methane Modeling (WAD2M), Zenodo, <https://doi.org/10.5281/zenodo.5553187>, 2021a.
- Zhang, Z., Fluet-Chouinard, E., Jensen, K., McDonald, K., Hugelius, G., Gumbricht, T., Carroll, M., Prigent, C., Bartsch, A., and Poulter, B.: Development of the global dataset of Wetland Area and Dynamics for Methane Modeling (WAD2M), *Earth Syst. Sci. Data*, 13, 2001–2023, <https://doi.org/10.5194/essd-13-2001-2021>, 2021b.
- Zhang, Z., Poulter, B., Feldman, A. F., Ying, Q., Ciais, P., Peng, S., and Li, X.: Recent Intensification of Wetland Methane Feedback, *Nat. Clim. Change*, 13, 430–433, <https://doi.org/10.1038/s41558-023-01629-0>, 2023.
- Zona, D., Gioli, B., Commane, R., Lindaas, J., Wofsy, S. C., Miller, C. E., Dinardo, S. J., Dengel, S., Sweeney, C., Karion, A., Chang, R. Y.-W., Henderson, J. M., Murphy, P. C., Goodrich, J. P., Moreaux, V., Liljedahl, A., Watts, J. D., Kimball, J. S., Lipson, D. A., and Oechel, W. C.: Cold Season Emissions Dominate the Arctic Tundra Methane Budget, *P. Natl. Acad. Sci. USA*, 113, 40–45, <https://doi.org/10.1073/pnas.1516017113>, 2016.